

**THE GROWTH, FABRICATION AND
CHARACTERIZATION OF HIGH PERFORMANCE
 $\text{Al}_x\text{Ga}_{1-x}\text{N}$ METAL-SEMICONDUCTOR-METAL
PHOTODIODES**

A THESIS
SUBMITTED TO THE DEPARTMENT OF PHYSICS
AND INSTITUTE OF ENGINEERING AND SCIENCE
OF BILKENT UNIVERSITY
IN PARTIAL FULFILLMENT OF THE REQUIREMENTS
FOR THE DEGREE OF
MASTER OF SCIENCE

By
Serkan Bütün
September 2006

I certify that I have read this thesis and that in my opinion it is fully adequate, in scope and in quality, as a dissertation for the degree of Master of Science.

Prof. Dr. Ekmel Özbay (Supervisor)

I certify that I have read this thesis and that in my opinion it is fully adequate, in scope and in quality, as a dissertation for the degree of Master of Science.

Asst. Prof. H. Volkan Demir

I certify that I have read this thesis and that in my opinion it is fully adequate, in scope and in quality, as a dissertation for the degree of Master of Science.

Asst. Prof. Vakur B. Ertürk

Approved for the Institute of Engineering and Science:

Prof. Dr. Mehmet Baray,
Director of Institute of Engineering and Science

Abstract

THE GROWTH, FABRICATION, AND CHARACTERIZATION OF HIGH PERFORMANCE $\text{Al}_x\text{Ga}_{1-x}\text{N}$ METAL-SEMICONDUCTOR- METAL PHOTODIODES

Serkan Bütün

M.S. in Physics

Supervisor: Prof. Dr. Ekmel Özbay

September 2006

High performance UV photodetectors have attracted unwarranted attention for various applications, such as in military, telecommunication, and biological imaging, as an $\text{Al}_x\text{Ga}_{1-x}\text{N}$ material system is also rather suitable for such applications. Its direct band gap covers the spectrum from 200 nm to 360 nm by way of changing the Al concentration in the compound. In this present thesis, the design and growth of an $\text{Al}_{0.75}\text{Ga}_{0.25}\text{N}$ template on sapphire substrate and a deep-UV photodiode with a cut off wavelength of 229 nm that was fabricated on the $\text{Al}_{0.75}\text{Ga}_{0.25}\text{N}$ template is presented. A responsivity of 0.53 A/W was attained corresponding to a detectivity of 1.64×10^{12} cmHz^{1/2}/W at a 50 V bias and 222 nm UV light illumination. The UV/VIS rejection ratio of seven orders of magnitude was achieved from the fabricated devices. The second work that was conducted in this thesis was the growth of a semi-insulating (SI-) GaN template. We also fabricated visible-blind photodetectors on this semi-insulating (SI-) GaN template. Furthermore, we fabricated identical samples on a regular GaN template in order to investigate any possible

improvement. The improvement found was obvious in terms of dark current. A dark current density of 1.96×10^{-10} A/cm² at a 50 V bias voltage for an SI-GaN photodetector was obtained, which is four orders of magnitude lower than devices on a regular GaN template. Devices on an SI-GaN had very high detectivity, and therefore, SI-GaN was used for low level power detection. The photogenerated current was well above the dark current that was under the illumination of just a few picowatts of UV light.

Keywords: Photodetector, Photodiode, GaN, AlGaIn, Metal-semiconductor-metal, Semi-insulating

Özet

YÜKSEK PERFORMANSLI $Al_xGa_{1-x}N$ METAL-YARIİLETKEN- METAL FOTODİYOTLARIN BÜYÜTÜLMESİ, ÜRETİLMESİ VE KARAKTERİZASYONU

Serkan Bütün

Fizik Yüksek Lisans

Tez Yöneticisi: Prof. Dr. Ekmel Özbay

Eylül 2006

Askeri, telekomünikasyon ve biyolojik görüntüleme gibi alanlar için yüksek performanslı mor-ötesi (MÖ) fotodedektörler her zaman önem arz etmektedir. $Al_xGa_{1-x}N$ malzeme sistemi bu tür uygulamalar için oldukça uygundur. Malzemenin doğru bant aralığı Al konsantrasyonu değiştirilerek 200 nm den 360 nm ye kadar olan bölge taranabilir. Bu çalışmada tasarımı yapıp safir üzerine büyüttüğümüz $Al_{0.75}Ga_{0.25}N$ katmanını ve bu katman üzerinde ürettiğimiz 229 nm kesme dalgaboyuna sahip derin MÖ fotodiyotları sunuyoruz. Üretilen fotodiyotlardan 50 V gerilim ve 222 nm MÖ ışık altında 0.53 A/W responsivite ve buna karşılık gelen $1.64 \times 10^{12} \text{ cmHz}^{1/2}/\text{W}$ dedektivite değerleri ölçüldü. On milyon kat mor-ötesi/görünür kontrastı elde edildi. Bu çalışmamızda değindiğimiz ikinci çalışma ise güneş-körü uygulamalar için düşük karanlık akımlı GaN fotodiyot üretimi idi. Bunun için önce safir üzerine bir yarı-yalıtkan GaN katmanı büyütüldü. Aynı zamanda karşılaştırma amacıyla başka bir GaN katmanı da geleneksel yöntemle büyütüldü. Neticede iki

fotodiyotun karanlık akımları karşılaştırıldı. Yarı yalıtkan malzeme üzerine büyütülen fotodiyotun dört bin kat daha az karanlık akım geçirdiği gözlemlendi. Bu düşük karanlık akım nedeniyle çok yüksek dedektivite değeri ölçüldü. Bu nedenle fotodiyot çok zayıf ışık sinyalleri altında denendi ve birkaç pW gibi düşük ışık tespit edilebildi.

Anahtar sözcükler: Fotodedektör, Fotodiyot, GaN, AlGaIn, Metal-yarıiletken-metal, Yarı-yalıtkan

Acknowledgements

I hereby present my sincere gratitude to my supervisor Prof. Dr. Ekmel Özbay for his endless support, guidance, motivation, and encouragement throughout this research. It was an experience of a lifetime and such a great honor to work with him.

I would like to specifically thank Dr. Mutlu Gökkavas for his help, and the valuable experience and suggestions that he shared with me, Dr HongBo Yu for his help on material growth, Mr. Erkin Ülker and Mr. Deniz Çalışkan for their valuable assistance on every matter.

I would like to thank all of the former and present personnel of the Nanotechnology Research Center for being great friends, having understanding, and making life much easier for me. My special thanks go to my office colleagues Mr. Turgut Tut and Mr. Bayram Bütün for their help with the laboratory equipment.

I would also like to thank all of the former and present personnel of the Advanced Research Laboratory and the Department of Physics. It was an honor to work alongside these rather hardworking people. Special thanks also go to Mr. Murat Güre and Ergun Kahraman for their technical support and guidance in the laboratory.

I would like to thank Asst. Prof. H. Volkan Demir and Asst. Prof. Vakur B. Ertürk for their being in my thesis committee.

Finally, I am indebted to my wonderful family for their continuous support and care.

Contents

Abstract	i
Özet	iii
Acknowledgements	v
Contents	vi
List of Figures	viii
List of Tables	x
1 Introduction	1
2 Theory	5
2.1 The Photodiode Operation.....	5
2.2 The Schottky Junction.....	6
2.3 The band gap of $\text{Al}_x\text{Ga}_{1-x}\text{N}$	8
2.4 Metal-Semiconductor-Metal Photodiodes.....	8
2.5 Photodetector Characterization.....	10
2.5.1 Current Voltage Characterization.....	10
2.5.2 Responsivity and Quantum Efficiency.....	11
2.5.3 Noise and Detectivity.....	12
3 Design and Growth	14
3.1 Metal-Organic Chemical Vapor Deposition (MOCVD).....	14
3.2 Material Design and Growth.....	16
3.2.1 $\text{Al}_{0.75}\text{Ga}_{0.25}\text{N}$ Design.....	16
3.2.2 $\text{Al}_{0.75}\text{Ga}_{0.25}\text{N}$ Growth.....	17
3.2.3 SI- and UD-GaN Wafer Design.....	20
3.2.4 SI- and UD-GaN Wafer Growth.....	23

4	Fabrication	28
4.1	Process Basics.....	28
4.1.1	Sample Preparation.....	29
4.1.2	Photolithography.....	30
4.1.2.1	Positive Photolithography.....	31
4.1.2.2	Image Reversal Photolithography.....	31
4.1.3	Etching.....	31
4.1.3.1	Dry Etching.....	32
4.1.3.2	Wet etching.....	32
4.1.4	Deposition.....	32
4.1.4.1	Metallization.....	33
4.1.4.2	Dielectric Coating.....	33
4.2	Device Fabrication Steps.....	33
4.2.1	Mesa Isolation.....	33
4.2.2	Schottky Contact Formation.....	34
4.2.3	Dielectric Coating.....	35
4.2.4	Interconnect Metallization.....	36
4.2.5	Lift-Off.....	36
5	Measurements	39
5.1	Experimental Results of Deep-UV Photodetectors.....	39
5.1.1	Current vs. Voltage Characteristics.....	39
5.1.2	Quantum Efficiency/Responsivity Measurements....	41
5.1.3	Noise Characterization.....	43
5.2	Experimental Results of Visible-Blind Photodetectors.....	45
5.2.1	Current vs. Voltage Characteristics.....	45
5.2.2	Responsivity Measurements.....	46
5.2.3	Low Power Photodetection.....	50
6	Achievements and Future Directions	52
	Bibliography	54

List of Figures

2.1	Schematic diagram of a simple photodiode operation.....	6
2.2	Schematic band diagram of a Schottky Contact. (a) before (b) after the contact formation.....	7
2.3	Schematic views of an MSM photodetector. (a) cross-sectional view (b) top view.....	9
3.1	Schematic diagram of the MOCVD reactor.....	15
3.2	Schematic diagram of the spectral transmission setup.....	19
3.3	Spectral transmission measurement of the $\text{Al}_{0.75}\text{Ga}_{0.25}\text{N}$ wafer.....	20
3.4	XRD $\omega/2\theta$ scan of the SI-GaN sample.....	23
3.5	XRD $\omega/2\theta$ scan of UD-GaN the control sample.....	24
3.6	Crystal quality improvement of SI-GaN over UD-GaN.....	24
3.7	Experimental setup of the photoluminescence measurement.....	25
3.8	PL measurement of the SI-GaN sample.....	26
3.9	PL measurement of the UD-GaN sample.....	26
3.10	PL comparison of the SI-GaN and UD-GaN templates.....	27
4.1	Sample before (a) and after (b) mesa isolation step.....	34
4.2	Schottky metallization.....	35
4.3	(a) Sample surface after dielectric coating, (b) Sample surface after wet etching with HF.....	35
4.4	Finalized device.....	36
4.5	Micrographs taken during the fabrication.....	38
5.1	IV Characteristics of a $100 \times 100 \mu\text{m}^2$ area device.....	40

5.2	IV Characteristics of a 4 μm finger width/spacing and 100 \times 100 μm^2 area device in a semilog scale.....	41
5.3	Schematic diagram of the Quantum efficiency setup.....	42
5.4	Spectral responsivity measurements of a 400 \times 400 μm photodetector.....	43
5.5	Experimental setup for noise measurements.....	44
5.6	Spectral noise measurement of a high-leakage 100 \times 100 μm photodetector with varying applied bias voltage.....	45
5.7	Current-voltage characteristics of 200 \times 200 μm MSM photodiodes with 10 μm /10 μm finger width/spacing on two different chips.....	46
5.8	Schematic diagram for a modulated spectral responsivity measurement.....	47
5.9	Measured spectral responsivity curves of 200 \times 200 μm devices with 3 μm /3 μm finger width/spacing on a UD-GaN sample.....	48
5.10	Measured spectral responsivity curves of 200 \times 200 μm devices with 3 μm /3 μm finger width/spacing on SI-GaN sample.....	49
5.11	Normalized modulated photoresponse of a 200 \times 200 μm device with 3 μm /3 μm finger width/spacing on the SI-GaN chip as a function of chopper frequency.....	50
5.12	Measured photocurrent of a 200 \times 200 μm device with 3 μm /3 μm finger width/spacing on the SI-GaN chip as a function of optical power and bias voltage. The dashed lines represent the adjustments to the plotted data.....	51

List of Tables

3.1	Epitaxial design of the $\text{Al}_{0.75}\text{Ga}_{0.25}\text{N}$ wafer.....	17
3.2	Epitaxial design of the semi-insulating GaN wafer.....	21
3.3	Epitaxial design of the unintentionally doped GaN wafer.....	21
4.1	Technical data sheet of the MSM photodetector fabrication.....	37

Chapter 1

Introduction

Ultraviolet (UV) spectrum corresponds to electromagnetic radiation with energy that is higher than 3.1 eV. Natural UV sources are mainly very hot objects, such as stars and flames. Developments in the past fifteen years have brought new artificial UV sources such as UV light emitting diodes [1-3] in addition to UV lamps. However, the most significant UV source is the sun. Most of the UV radiation on earth is due to solar radiation. Normally, UV radiation is very harmful to life. Fortunately, the ozone layer absorbs the UV radiation with $\lambda < 280$ nm, which is called the solar blind region. Therefore, there is no natural radiation for $\lambda < 280$ nm within the atmosphere. Hence, it is even more important to make a detector that is sensitive for $\lambda < 280$ nm because the source will be an extraordinarily hot object if there is radiation within the atmosphere [4]. Similarly, the radiation above the visible region of the electromagnetic spectrum is called the visible-blind region ($\lambda < 400$ nm) because the human eye does not respond to the wavelengths smaller than 400 nm.

These two regions are named after the natural cut offs. There are also standards that are given to the various portions of the UV spectrum such as, near UV (400 nm – 320 nm), mid-UV (320 nm – 260 nm), and deep UV (260 nm – 190 nm). The region below the deep UV portion is called vacuum UV because the atmosphere absorbs below 190 nm.

There are numerous applications of UV generation and detection. For the generation part we have UV LEDs and lasers for UV photolithography, high density optical storage, non-line of sight communication systems, true color displays etc... Detection of the UV spectrum has a wide range of applications such as in the military, environmental, scientific, telecommunication, and industrial areas. For instance, from a scientific point of view, we have chemical and biological agent detection [5], as well as exposure monitoring. The UV photodetectors can be used for ozone layer monitoring (environmental) and missile plum detection and non-line of sight communication systems (military), as well as flame and heat engine monitoring (industry)[6].

Conventionally, UV photodetection is performed by photomultiplier tubes (PMTs), thermal sensors, and narrow band-gap semiconductor diodes. The detectivity values for PMTs can be very high, and can exhibit very low noise because there is no contact material between the electrodes. However, PMTs are made out of a vacuum tube and are very delicate. They require very high bias voltages (on the order of kV) and are rather expensive. Moreover, they are sensitive to all wavelengths, and for this reason they specifically require designed filters in order to operate at certain wavelengths [6-7].

Solid state photodetectors on the other hand are small in size, easy to fabricate, and inexpensive. They are suitable for integrated circuits and high speed applications. Si was the first material ever used for UV photodetection because of its well established technology. However, Si and other narrow band gap materials have the same problem with PMTs. They also require expensive filters in order to operate at certain regimes of electromagnetic radiation [6-7].

Developments in the past fifteen years have shown that $\text{Al}_x\text{Ga}_{1-x}\text{N}$ based materials are especially suitable for detecting the UV spectrum, since the band gap of $\text{Al}_x\text{Ga}_{1-x}\text{N}$ material covers the entire mid-UV and near-UV spectrum. Its band gap can be precisely selected by varying the Al concentration from 200 nm to 360 nm. The most important feature is that it is intrinsically visible blind, and therefore, it does not require any complex filters. The material is highly robust

(in fact it is one of nature's hardest materials) and insensitive to magnetic fields. Since it is a direct band gap semiconductor it exhibits a sharp cut off and high absorption near the band edge [8].

Various types of $\text{Al}_x\text{Ga}_{1-x}\text{N}$ based photodetectors have been reported after the first successful demonstration of UV photodetectors [9-10], such as the Schottky barrier [11-12], p – i – n [13-15], and MSM [16-18] photodetectors. The highest Al concentration in those photodetectors was 50% and had a ≥ 260 nm cut-off wavelength. There are only a few low cut-off wavelength photodetectors that are reported in the literature [19] because of the growth difficulties of high quality and crack-free high Al content material. Razeghi *et al.* reported the best results with a cut-off wavelength of 235 nm [20].

Structures with high Al content exhibited low dark current values. However, photodetectors on GaN material have relatively high dark current levels that were on AlGaN. There have only been a few reports regarding relatively low dark current devices that were fabricated on GaN. The best result was around 10 pA at a 100 V bias [21].

The motivation behind this work was the need for low cut off wavelength photodetectors for deep UV applications and color sensing. Moreover, the current status of GaN based photodetector technology is insufficient for some applications such as photon counting. There is always a need for more sensitive devices.

In this present work, one of our aims was to first grow a high quality, crack free, and high Al concentration epitaxial layer, and second, to demonstrate a deep UV photodetector by fabricating and testing an MSM structure on it. The second aim decreases the dark current of GaN based photodetectors by utilizing the idea that was used for high electron mobility transistors. A semi-insulating (SI) GaN layer is used instead of a regularly grown GaN.

All the design, growth, fabrication, and characterization processes were performed at Bilkent University, except for the x-ray diffraction measurements. They were performed in the Semiconductor Technologies Advanced Research

Laboratory at Gazi University. Growth of the epitaxial layers was performed at the Nanotechnology Research Center, and the other parts were performed at the Advanced Research Laboratory at Bilkent University.

Chapter 2 covers the theoretical background of photodiode operation and a brief explanation of the Schottky junction. Then, it summarizes the figures of merit for the photodetector characteristics, such as current-voltage behavior, spectral response, and noise characteristics.

In chapter 3 we present the issues that are related to the design of the epitaxial layers and the growth processes. It is divided into two parts. The first part is devoted to $\text{Al}_{0.75}\text{Ga}_{0.25}\text{N}$ epitaxial growth. The second one is devoted to two GaN wafers. We also represent some wafer characterization results after we performed the growth, such as transmission, x-ray diffraction, and photoluminescence measurements.

Chapter 4 explains the fabrication techniques of the MSM photodetector. It starts with the basic microfabrication steps and methods, and then goes on to the actual steps of the fabrication of our photodiodes along with the technical details.

The characterization results are presented in chapter 5. This chapter is also divided into two parts. The first part reveals the IV results, spectral response, and noise characterization of a deep UV photodiode. The second part is about the characterization results of the visible-blind photodetectors.

We summarize our results in chapter 6 by providing the results of our fabricated photodiodes. At the end, we mention our achievements and the possible future research directions.

Chapter 2

Theory

In this chapter, we present the basic background of photodiode operation in the beginning. Thereafter, we discuss the Schottky junction, which is the only junction in our photodetectors. Then, the basic operation of the metal semiconductor metal (MSM) is described. Finally, the main figures of merit, which are used to characterize a photodetector, will be discussed.

2.1 The photodiode operation

Photodiodes currently are the most frequently used photodetectors in industry because of their efficiency and low cost. A standard simple photodiode has semiconductor material and some junctions such as metal-semiconductor (Schottky), *p-n*, and *p-i-n*. The main mechanism is the following; when photons that have energy ($h\nu$) that is higher than the band gap of the semiconductor (E_G) incident up on the junction are absorbed. They produce electron-hole pairs in the depletion region. If a sufficient electric field is applied (in this case if there is a bias) through the depletion region, the charged carriers then produce a measurable electric current (I_{ph}). Therefore, it is required that a photodiode must be reversely biased (V_B) in order to work. Figure 2.1 schematically explains the operation of a simple diode [22-23].

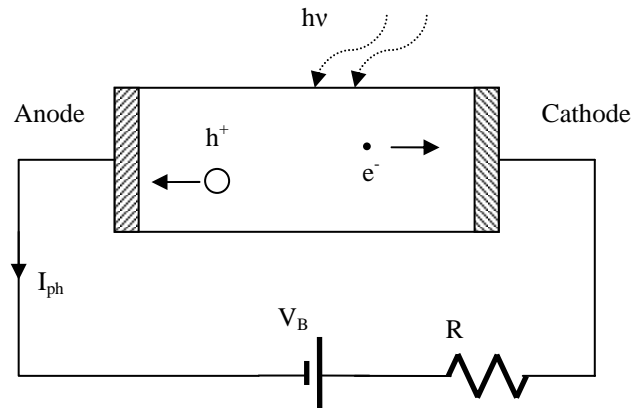


Figure 2.1: Schematic diagram of a simple photodiode operation.

2.2 The Schottky Junction

The Schottky junction (also known as a metal-semiconductor junction) is made up of a metal and a semiconductor material. The name was taken from *Walter H. Schottky* who explained the rectifying behavior of this type of contact in 1930.

Making a Schottky contact (junction) is relatively easy. Depositing a metal on a semiconductor is sufficient to create them. Unfortunately, it is not possible to make a perfect Schottky barrier contact with just any metal placed on a certain semiconductor. Some metals tend to diffuse into the semiconductor. Eventually, the rectifying behavior of the contact disappears.

When a metal is deposited on a semiconductor, a phenomenon called Fermi Level Pinning occurs. [24] That is, in thermal equilibrium, the Fermi levels of each material should be equal. The band diagram of a Schottky contact is shown in figure 2.2.

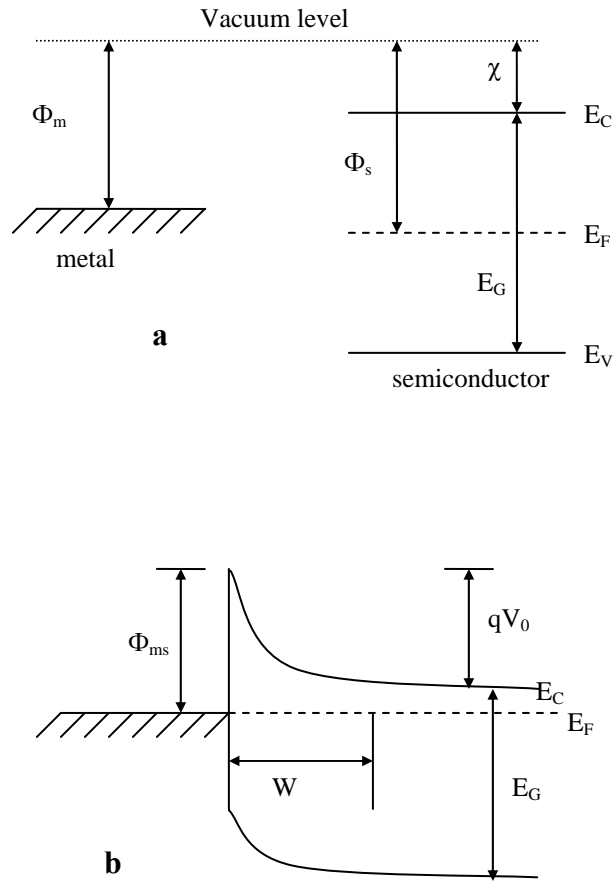


Figure 2.2: Schematic band diagram of a Schottky Contact. (a) before (b) after the contact formation.

The work function is defined as the difference between the vacuum and Fermi levels denoted as Φ_m and Φ_s for metal and semiconductor, respectively. Here χ represents the electron affinity of the semiconductor. Then, for an ideal contact the barrier height is given as

$$\Phi_{ms} = \Phi_m - \chi \quad (2.1)$$

Additionally, the contact potential qV_0 is given as

$$qV_0 = \Phi_{ms} - (E_C - E_F) \quad (2.2)$$

Using the abrupt junction approximation, we conclude that the depletion layer width is given as [23],

$$W = \sqrt{\frac{2\varepsilon}{qN_D} \left(V_0 - V - \frac{k_B T}{q} \right)} \quad (2.3)$$

where ε is the dielectric constant and N_D is the n-type donor density of the semiconductor. Here, V denotes the applied bias voltage to the junction.

There are four main mechanisms for current transportation in a Schottky barrier, such as thermionic emission, tunneling, recombination/generation in the depletion region, and recombination/generation in a neutral region. The main transport mechanism is the thermionic emission over the barrier also produces the ideal diode characteristics to the junction. Crowell and Sze proposed the expression for the I-V characteristics of a Schottky barrier junction.

$$I = I_S \left(e^{\frac{qV}{kT}} - 1 \right) \quad (2.4)$$

$$I_S = A^{**} T^2 e^{-\frac{q\Phi_{ms}}{kT}} \quad (2.5)$$

where A^{**} is the effective Richardson constant.

2.3 The Band-gap of $\text{Al}_x\text{Ga}_{1-x}\text{N}$

The band gap of $\text{Al}_x\text{Ga}_{1-x}\text{N}$ with respect to Al concentration x is calculated with the empirical formula

$$E_g = xE_{g,AlN} + (1-x)E_{g,GaN} - bx(1-x) \quad (2.6)$$

where b ($0 < b < 1$) is the bowing parameter that is measured experimentally. There are a number of values for b reported in the literature [25 and references therein]. In this present work we used $b = 0.62$ eV.

2.4 Metal-Semiconductor-Metal Photodiodes

MSM photodiodes are one of the simplest photodetectors in terms of epitaxial growth and fabrication. They are formed by two back to back Schottky

junctions on a semiconductor surface. When a bias is applied, one of the junctions becomes reversed and the other one becomes forward. Since it is a unipolar device one of the junctions will always be reverse biased. Therefore, current is not allowed to pass in each direction. [3]

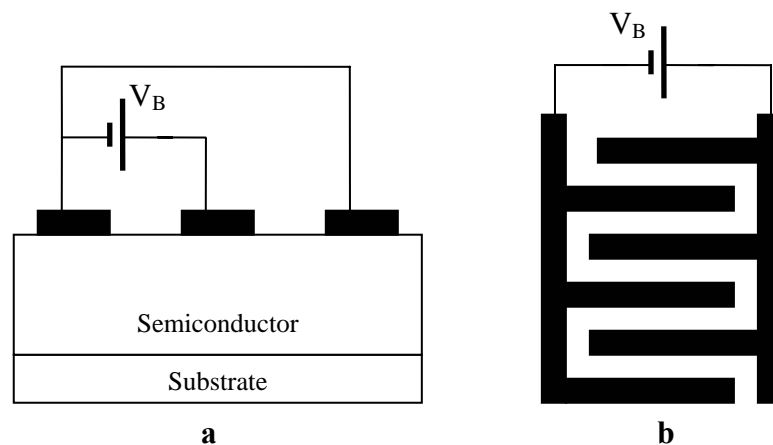


Figure 2.3: Schematic views of an MSM photodetector. (a) cross-sectional view (b) top view.

There is a certain limit for the electric field that can be applied through the semiconductor. Moreover, depleting the carriers between the electrodes is important. Therefore, high bias voltages sometimes are required for the depletion of the entire area. In order to overcome these issues and efficiently collect the incident radiation, the metal electrodes are often interdigitated (see figure 2.3). Interdigitated fingers also reduce the carrier transit time, and therefore, the speed of the device increases.

MSM photodiodes are very easy to realize, especially in materials such as AlGaIn/GaN. Due to growth complexities, it is rather difficult to grow complex epitaxial structures. Contrarily, MSM devices only require a single epitaxial layer. Moreover, the fabrication of these kinds of devices is

straightforward. They are compatible with integrated circuit processing and are suitable for high speed applications. Although these rather nice properties exist, there is another issue about the basic properties of metals. Metals are very good reflectors of electromagnetic radiation. In addition, the skin depth values for metals are rather low (~15-20 nm). Therefore, in MSM structures, nearly half of the light can go through the semiconductor. There are two possible solutions to this problem. The first one is to make the electrodes as thin as possible so they can transmit as much light as possible. This is also the method we used in this present work. The other method is the back illumination of the device. However, in this case your substrate and underlying layers should also be transparent to the incident radiation.

2.5 Photodetector Characterization

Commonly defined figures of merit exist for detector characterization. These are current voltage, quantum efficiency and responsivity, noise and detectivity, and time response characteristics [8, 22-24]. Here we will discuss current voltage, quantum efficiency and responsivity and noise and detectivity characteristics which were carried out in this present work.

2.5.1 Current-Voltage Characterization

The main current-voltage behavior of a diode depends on the type of junction used. Although MSM structures have a Schottky junction inside, we cannot see the real Schottky behavior in the I-V curve. What we can see is just the reverse bias characteristics. Equation 2.4 represents the ideal forward current voltage relation of a Schottky junction. However, there is a correction to that equation as

$$I = I_S \left(e^{\frac{qV}{nkT}} - 1 \right) \quad (2.7)$$

where n is the ideality factor ($n \geq 1$). If $n = 1$, this means that we only have a thermionic emission. Otherwise, the other carrier transport mechanisms are involved.

I_s in the equation is ideally the reverse saturation current of the diode. The MSM structures equation 2.5 is insufficient to explain the reverse current characteristics. We have to include the hole components as well, because there are two diodes and one of them is in forward bias. The overall expression for dark current is therefore

$$I = A_n^* T^2 e^{-\frac{q\Phi_{ms}^n}{kT}} + A_p^* T^2 e^{-\frac{q\Phi_{ms}^p}{kT}} \quad (2.8)$$

where A_n^* and A_p^* are effective Richardson constants for electrons and holes, respectively. Φ_{ms} values also differ for the different carrier types.

2.5.2 Responsivity and Quantum Efficiency

The quantum efficiency of a photodetector is defined as the probability of generating an electron-hole pair that will contribute to the photocurrent by way of a single photon. It is a wavelength dependent quantity and is expressed conventionally as

$$\eta(\lambda) = (1 - R)(1 - e^{-\alpha(\lambda)d}) \quad (2.9)$$

where R is the reflectivity of the top surface, $\alpha(\lambda)$ is the absorption coefficient and d is the absorptive layer thickness. Efficiency increases with an increasing absorption layer thickness. However, thick layers cause longer carrier transit times. Therefore, the detector is slower. This phenomenon is called the efficiency-bandwidth trade off. Furthermore, efficiency drops rapidly when λ becomes larger than the corresponding band gap wavelength.

Responsivity is another measure to characterize a photodetector. It is defined as the outcome produced (current or voltage) per incident optical power.

Therefore, it usually has the units A/W or V/W. The responsivity is related to the quantum efficiency as

$$R(\lambda) = \frac{I_{ph}}{P} = \frac{\eta e}{h\nu} = \eta \frac{\lambda(nm)}{1240} \quad (2.10)$$

2.5.3 Noise and Detectivity

The current generated by a photodiode is not always due to an optical source. There are other effects that produce random currents, mainly noise.[22] There are three sources of noise mainly. The first one is Shot noise and is due to the random generation of carriers across the potential barriers. The frequency dependent Shot noise current is given as

$$\langle i_s^2(f) \rangle = 2q\langle I \rangle \Delta f \quad (2.11)$$

where $\langle I \rangle$ is the dark current and Δf is the bandwidth. The second important noise is the thermal (Johnson) noise. It is mainly from the random thermal movements of the carriers and is given as

$$\langle i_t^2 \rangle = 4k_B T \frac{\Delta f}{R} \quad (2.12)$$

where R is the differential resistance. The final and most dominant noise in our detectors is the $1/f$ (flicker) noise, which is related to trap centers in both bulk or surface and leakage currents. The $1/f$ noise is defined as

$$\langle i_{1/f}^2 \rangle = k_B \langle I \rangle \frac{\Delta f}{f} \quad (2.13)$$

As one can see from the above expressions, at high frequencies and high bandwidths, shot noise is dominant but at low frequencies, 1/f noise becomes dominant.

There is another quantity called noise equivalent power (NEP) and is defined as the minimum optical power required for producing a photocurrent that will give unity in the signal to noise ratio. NEP is given by

$$NEP = \frac{I_n}{R} \quad (2.14)$$

I_n is the total noise (i.e. the root mean square of the sum of the three noises provided above), in which R is the responsivity.

Generally, NEP is a small quantity and the smaller the NEP the better the detector. Therefore, another quantity called Detectivity is defined as the inverse of the NEP. More specifically, the detectivity per area is called specific detectivity (D^*) and is also defined as

$$D^* = \frac{\sqrt{A\Delta f}}{NEP} \quad (2.15)$$

where a is the device active area. The unit of the D^* is $\text{cmHz}^{1/2}/\text{W}$. There is also another way to calculate D^* , [26] which is called a thermally limited detectivity formula,

$$D^* = R_\lambda \left(\frac{R_0 A}{4kT} \right)^{1/2} \quad (2.16)$$

where A is the device area, R_λ is the device responsivity, and R_0 is the differential resistance at a corresponding voltage. R_λ and R_0 are measured at a 0 V bias.

Chapter 3

Design and Growth

In this chapter, we first provide the fundamental MOCVD background. Topics such as what are the basic parts and basic operation will be covered. Then, we will move on to the design of our wafers. Finally, we explain in detail the growth process of our wafers.

3.1 Metal-Organic Chemical Vapor Deposition (MOCVD)

Crystal growth is one of the key aspects for the realization of any semiconductor device. It is important to grow high quality and crack free heterostructures with different layers of materials and specific doping concentrations as well as the growth of high quality single layer crystals in order to make high performance electronic devices [27]. The first successful demonstration of III-V compound growth using metalorganic precursors and hydride sources was reported in 1960 by Didchenco *et al.* Later, the technique was improved and given the name MOCVD (Metal Organic Chemical Vapor Deposition), also called MOVPE

(Metal Organic vapor phase epitaxy). Before that, MBE (Molecular Beam Epitaxy), VPE (Vapor Phase Epitaxy), and LPE (Liquid Phase Epitaxy) were used. Metal Organic Chemical Vapor Deposition (MOCVD) is one of the two key enabling technologies that is critical for growing the heterostructures of III-V compounds (MBE is the other). MOCVD relies on metal-organic compounds, such as trimethyl gallium or trimethyl aluminum, which acts as a precursor for the material in thin films. The materials that are grown contain some combinations of gallium, indium, aluminum, nitrogen, phosphorus, or arsenic. The process consists of transporting the precursors via a carrier gas (in our case H_2) to a hot zone within a growth chamber. These precursors either dissociate or react with another compound to produce thin films consisting of a single element or compound. Varying the composition of the deposited materials, and doping in the epilayers, produces the end structure.

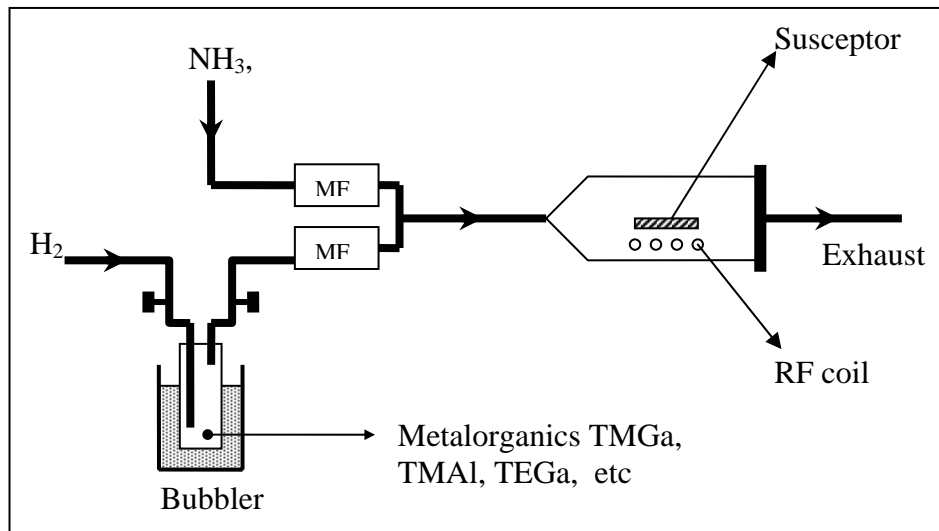


Figure 3.1: Schematic diagram of our MOCVD reactor.

The MOCVD system, in which we grow our samples, is located at the Bilkent Nanotechnology Research Center and is an AIXTRON RF200/4 RF-S GaN/AlGaN horizontal flow low pressure MOCVD system. It is composed of three main parts; the Gas Mixing Cabinet (GMC), Reactor Cabinet (RC), and E-

Rack. In addition to these, we have a hydride source NH_3 , SiH_4 as an n type dopand, and metalorganic sources such as trimethylgallium (TMGa), trimethylaluminum (TMAI), triethylgallium (TEGa) for III sources, and bis-cyclopentadienylmagnesium (Cp_2Mg) as a p type dopand.

GMC is where we arrange all the required combinations of gas mixtures that we sent previously to the reactor. The epitaxial films are produced according to the concentration of each individual molecule in this mixture. GMC consists of many electronically controlled mass flow controllers and pneumatic three way valves, which are used to adjust the gas mixture concentration. RC is where the reaction and deposition occur. It consists of a vacuum chamber, radiofrequency (RF) coil, rotary pump, antechamber, and susceptor. Using an RF generator, we control the temperature of the susceptor, and therefore, the reaction. We can heat the susceptor up to $1,200^\circ\text{C}$. The pump helps us to regulate the pressure inside the reactor. The antechamber is for loading and unloading the wafers. The susceptor is the part where we place our wafers. Finally, the E-Rack is the component that has all the electronic control units. It is controlled by a computer with which we write the relevant recipes and control the reaction.

3.2 Material Design and Growth

3.2.1 $\text{Al}_{0.75}\text{Ga}_{0.25}\text{N}$ Design

An $\text{Al}_x\text{Ga}_{1-x}\text{N}$ material system exhibits a band gap from 3.6 to 6.2 eV with increasing x. This corresponds to a wavelength interval between 200 and 360 nm. In order to make a photodetector sensitive in the deep-UV region we need to grow AlGa_N templates with a very high Al concentration. It is very difficult to grow high quality, crack free even single layer templates with this much Al concentration. Rather little research has been conducted by other groups on this high of an Al concentration in the AlGa_N layers that were reported in the

literature [19-20]. Our aim was to construct a simple MSM photodetector, and therefore, we do not need any complex heterostructures other than a single layer high quality AlGa_{0.25}N layer.

There is a ~10% lattice mismatch between sapphire and AlGa_{0.25}N. Because of that, an AlGa_{0.25}N epitaxial layer cannot be grown directly on sapphire substrate. Even if we manage to avoid cracks, many dislocations that will act as trap centers for carriers will in turn increase an unintentional doping concentration, which will increase the leakage current. Therefore, it is customary to introduce mid layers such as a nucleation and buffer layer between the substrate and epitaxial layers. You can see our epitaxial design shown in table 3.1. These additional layers reduce the horizontal strain due to the lattice mismatch, and increase the crystal quality of the top layer.

Layer	Material	Thickness (nm)
Active	Al _{0.75} Ga _{0.25} N	700
Buffer	AlN	600
Nucleation	AlN	50
Substrate	Sapphire	3.3×10^5

Table 3.1: Epitaxial design of the Al_{0.75}Ga_{0.25}N wafer.

3.2.2 Al_{0.75}Ga_{0.25}N Growth

A high quality Al_{0.75}Ga_{0.25}N epitaxial layer was grown in an MOCVD system located at Bilkent University on double sided polished c-plane sapphire substrate. These sapphire substrates are commercially available from a number of companies throughout the world. Prior to the growth, we increased the wafer temperature to 1,100°C and decreased the pressure to 10 mbar for desorption for 10 minutes. During the desorption, any undesired materials deposited, such as dirt on the sapphire substrate, evaporates and washes out by way of H₂ purging gas. This step is mainly aimed at cleaning and preparing the sapphire substrate

for growth. The H_2 purging flow rate was maintained at 8500 sccm during this step. After desorption, the reactor was cooled to 840°C to grow a thin (~ 50 nm) AlN nucleation layer. H_2 was used as a carrier gas throughout the entire growth process. The TMAI and NH_3 flow rates were 20 sccm and 1000 sccm, respectively. At this temperature, Al and N atoms grew as an amorphous layer on the sapphire. Afterward, we heated up the reactor at approx. $1,150^\circ\text{C}$ for 10 minutes in order to make that amorphous layer a single crystal layer. Since the layer is rather thin; Al and N atoms can easily align themselves as a wurtzite structure. The nucleation layer helps to overcome the lattice mismatch problem of the AlGaIn material system and sapphire substrate. After the growth of the nucleation layer a 700 nm high temperature AlN buffer layer was grown at approx. $1,140^\circ\text{C}$. The flow rates of TMAI and NH_3 were adjusted to 40 sccm and 150 sccm, respectively. This buffer layer reduces the strain effects as we grow away from the sapphire. Finally, we grew an unintentionally doped 600 nm thick $Al_{0.75}Ga_{0.25}N$ active layer. The growth conditions were as follows. The reactor temperature was set to 800°C and the flow rates were 15 sccm, 5 sccm, and 300 sccm for TMAI, TMGa, and NH_3 , respectively. When the growth of the active layer was finished, we started cooling the reactor to room temperature. While cooling, we kept the NH_3 flow on the surface of the wafer. This ammonia flow helps prevent crack formation, and in a way also polishes the surface of the wafer.

To check the Al concentration of our wafer we performed a spectral transmission measurement. We know that sapphire is transparent in the UV range and the band gap of AlN is 6.2 eV, which corresponds to an absorption edge of approx. 200 nm. Therefore, we can see the absorption edge of the $Al_{0.75}Ga_{0.25}N$ layer exactly with the spectral transmission measurements. Using equation 2.6 with the measured absorption band edge, and therefore, band gap energy, we can determine the exact concentration of the Al in the active layer.

We used an Ocean Optics Chem2000-UV-VIS PC Plug-in Fiber Optic Spectrophotometer for the spectral transmission/reflection setup, a schematic of

which is shown in figure 3.2. We have an Xe arc lamp for the UV source. We collimated the output of the lamp by a UV enhanced collimating lens to a multimode UV enhanced fiber by which we illuminated our sample. We have another collimator after the sample, which collects the transmitted light. Finally, we have a spectrometer that consists of a grating and CCD array.

Figure 3.3 shows the performed spectral transmission measurement of our wafer before the fabrication of the MSM photodetectors. The results indicate a 225 nm sharp cut-off, which corresponds to a band gap of 5.51 eV. Using the equation 2.6 we found an Al concentration of approximately 75%.

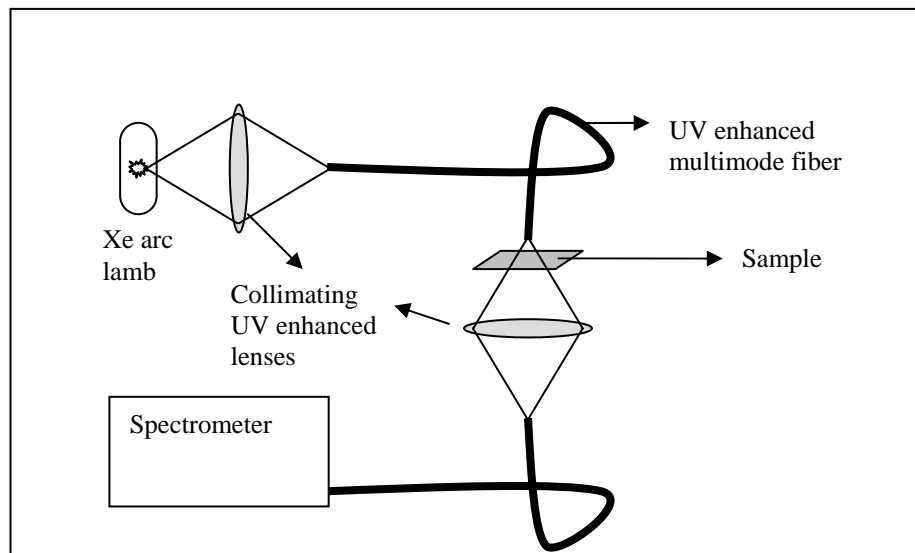


Figure 3.2: Schematic diagram of our spectral transmission setup.

As you can see from figure 3.3, for a wavelength larger than the cut-off, we have the Fabry-Perot oscillations that result from the microcavity that is formed by the two epitaxial layers on sapphire. These oscillations are a good sign of the quality of the surface and the bulk itself.

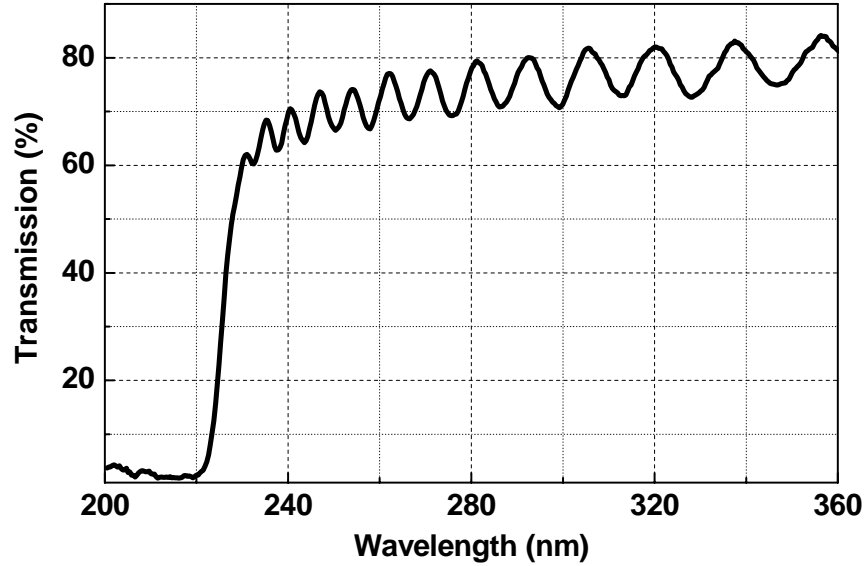


Figure 3.3: Spectral transmission measurement of the $\text{Al}_{0.75}\text{Ga}_{0.25}\text{N}$ wafer.

3.2.3 SI- and UD-GaN wafer design

In order to overcome the relatively high leakage problem in GaN over AlGaN templates there has been a number of studies conducted, such as the introduction of a thin AlGaN cap layer deposition on the GaN active layer. This method, however, again suffers from the polarization effects due to the interface between the GaN and AlGaN layers. Therefore, it may not be easy to establish good Schottky contacts on that kind of structure.

We introduced the method that is used in high electron mobility transistors on GaN. This method introduces a semi-insulating GaN buffer layer such that the source-drain leakage is minimized.

Semi-insulating indicates the high crystal quality of the template, which means that we have fewer dislocations in the epitaxial layer, which corresponds to higher resistivity values. The detectivity of a photodetector is directly proportional to the square root of the differential resistance. (See equation 2.16).

Hence, if the resistivity is high, then the detectivity will also be high. One other point is that the leakage current (sometimes called dark current) is lowered when the resistivity is high. It is crucial that the leakage current is very low in order to identify the signal coming from a very weak source. With the intention of high performance such as in single photon detection, leakage current must be much lower than the photocurrent, which can be generated by a single photon.

To achieve a better quality GaN crystal, we introduced an AlN buffer layer under the GaN active layer. When growing regular GaN on sapphire we must introduce a nucleation layer in order to overcome a nearly 16 percent lattice mismatch. However, yet again this nucleation layer is insufficient to grow superior quality crystals. Lattice mismatch between GaN and AlN is somewhat easy to handle (about 3 percent). Therefore, using an AlN as a buffer layer might improve the quality of the GaN crystal. We also grew a regular unintentionally doped GaN again on another sapphire substrate for comparison. (See tables 3.2 and 3.3)

Layer	Material	Thickness (nm)
Active	GaN	500
Buffer	AlN	500
Nucleation	AlN	15
Substrate	Sapphire	3.3×10^5

Table 3.2: Epitaxial design of the semi-insulating GaN wafer.

Layer	Material	Thickness (nm)
Active	GaN	500
Nucleation	GaN	50
Substrate	Sapphire	3.3×10^5

Table 3.3: Epitaxial design of the unintentionally doped GaN wafer.

3.2.4 SI- and UD-GaN Wafer Growth

The samples in this study were all grown again on c-face (0001) sapphire substrates by low-pressure MOCVD. Hydrogen was again used as the carrier gas, in which TMGa, TMAI, and NH_3 were used as the Ga, Al, and N sources, respectively. An SI-GaN layer was grown on high temperature AlN buffer. Prior to the epitaxial growth, sapphire substrates were annealed for desorption at $1,100^\circ\text{C}$ for 10 min to remove surface contamination (the details of which were discussed in previous chapters). We started our growth process with a 15nm-thick AlN nucleation layer. To do that, we adjusted the temperature to 840°C . Then, the flow rates of TMAI and NH_3 were set to 15 sccm and 300 sccm, respectively. Thereafter, the reactor temperature was ramped to $1,150^\circ\text{C}$ in order to make the amorphous material crystalline. The next step was the AlN buffer layer. Basically, we continued to grow AlN as in the nucleation layer but at not the same temperature. During the growth of these two processes the reactor pressure was 200 mbar. Subsequently, we had a two minute growth interruption in order to reach the optimum growth conditions for GaN. The growth conditions of GaN were as follows: reactor pressure 200 mbar, growth temperature $1,070^\circ\text{C}$, growth rate at an approx. $2\mu\text{m/h}$ of the flow rate of TMGa 15 sccm and the flow rate of NH_3 were ramped from 200 sccm to 1300 sccm during the growth. We finished the growth as described previously.

A typical UD-GaN control sample was also grown on sapphire substrate. We used the two-step method. First a 50 nm low temperature GaN nucleation layer was deposited at 500°C . Then, the reactor temperature was ramped up to $1,070^\circ\text{C}$. After that, a 500 nm GaN layer was grown. For a fair comparison, the thickness and growth parameters of the high temperature GaN (HT-GaN) layer were selected in the same way as in the previous growth.

We performed a series of measurements in order to compare these two GaN wafers. Two different types of measurements were utilized for the x-ray diffraction (XRD) and photoluminescence (PL) measurements. Both of these

experiments were proof for the grown GaN crystal, in which they provided the information that was related to the crystal quality of our wafers.

XRD measurements were performed in the Semiconductor Technologies Advanced Research Laboratory, Gazi University, Ankara. Since our claim was that the SI-GaN crystal is a better crystal in terms of quality than the UD-GaN crystal, we expected that SI-GaN would result in a narrower XRD peak.

Figure 3.4 and 3.5 demonstrate the XRD $\omega/2\theta$ scan measurement results. You can clearly see GaN and AlN peaks on each relevant figure. We plotted the experimental data of the GaN peak in one figure (figure 3.6) in order to see the improvement. As you can see in figure 3.6 we obtained a rather good enhancement in terms of crystal quality. The UD-GaN, which was grown using the standard two step method, had a FWHM as 199 arcsec, whereas the SI-GaN sample had a FWHM of 118 arcsec. These measurements were clearly a sign proving the better quality of the SI-GaN.

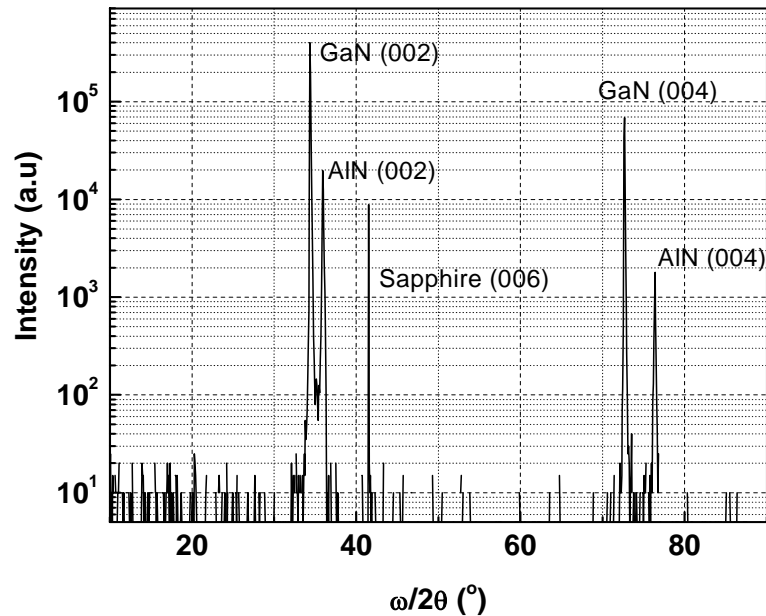


Figure 3.4: XRD $\omega/2\theta$ scan of SI-GaN sample.

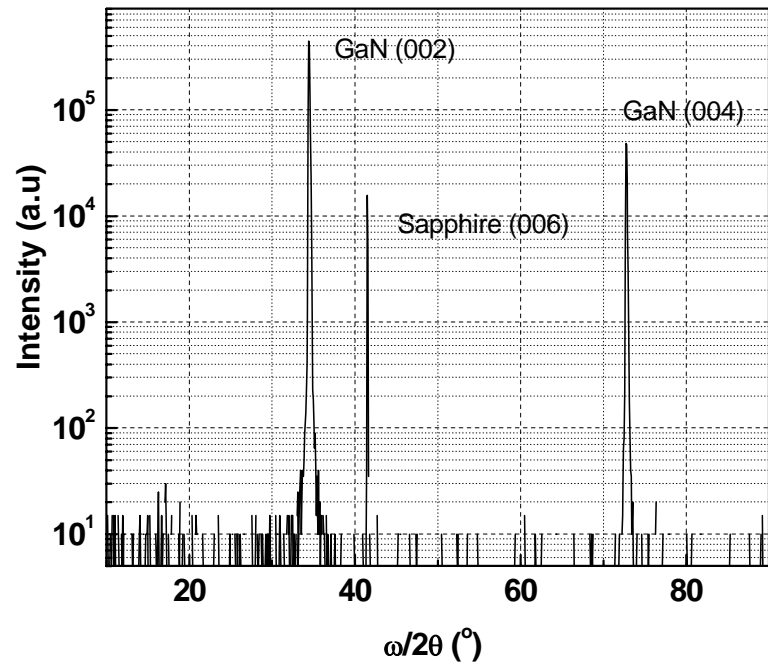


Figure 3.5: XRD $\omega/2\theta$ scan of UD-GaN control sample.

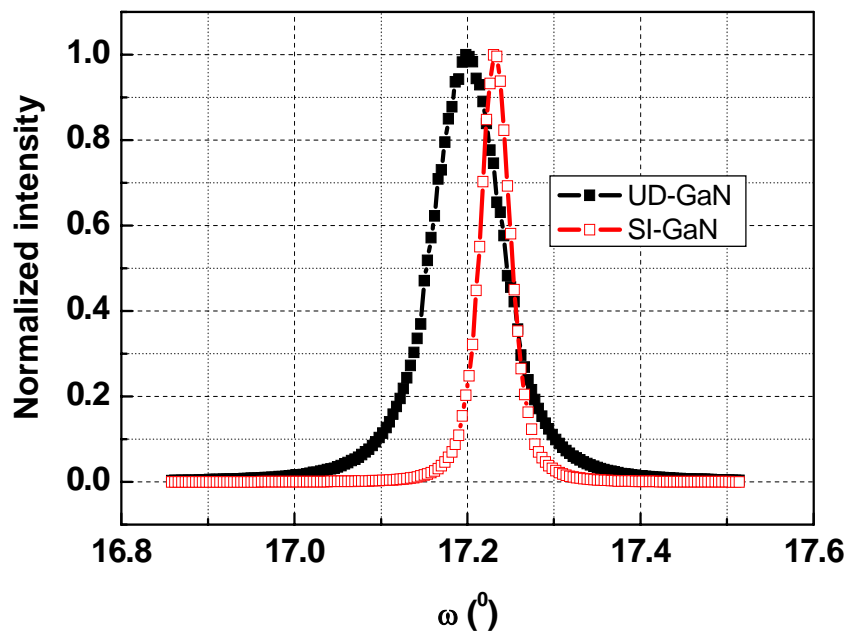


Figure 3.6: Crystal quality improvement of SI-GaN over UD-GaN.

We also performed a PL measurement on both samples. Figure 3.7 shows our experimental setup. We concluded from the following figures (figure 3.8 and 3.9) that we obtained no other crystal or quantum structure that had a band transition energy that was lower than GaN. We could not see the peak of AlN in SI-GaN because the wavelength of our laser is 325 nm, which has energy that is well below the bulk transition energy of AlN. Therefore, we expected no detectivity from our devices above 360 nm.

We also compared the two PL curves of the two samples in a more detailed semilog scale plot (see figure 3.10). As you can see, both of the samples exhibited good results in terms of PL. The FWHM values are 4 nm and 6 nm with the peak wavelengths of 361 nm and 362 nm for SI-GaN and UD-GaN, respectively.

Both XRD and PL measurements are proof enough that we achieved good quality GaN crystals even for UD-GaN, which was grown using the standard two step method. On the other hand, our SI-GaN showed signs of better quality than UD-GaN in terms of these measurements.

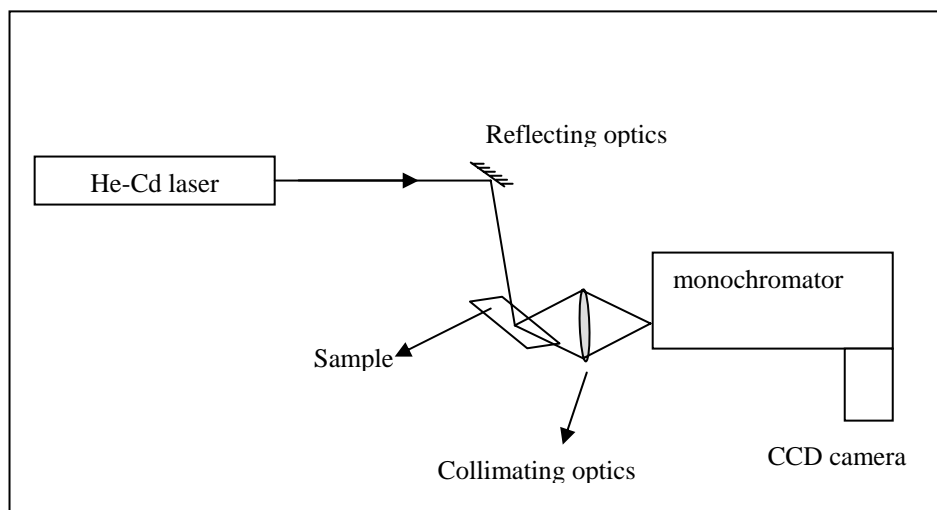


Figure 3.7: Experimental setup of our photoluminescence measurement.

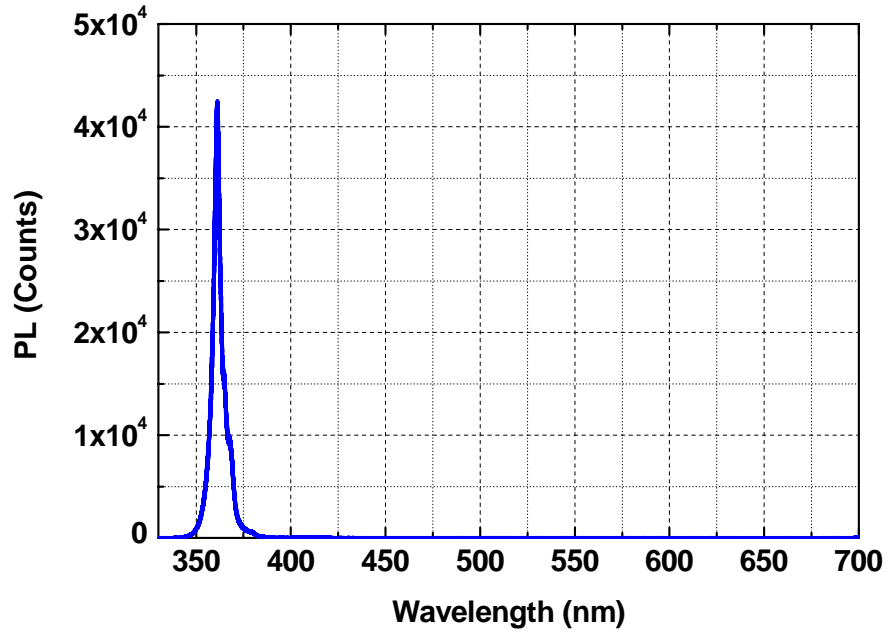


Figure 3.8: PL measurement of the SI-GaN sample.

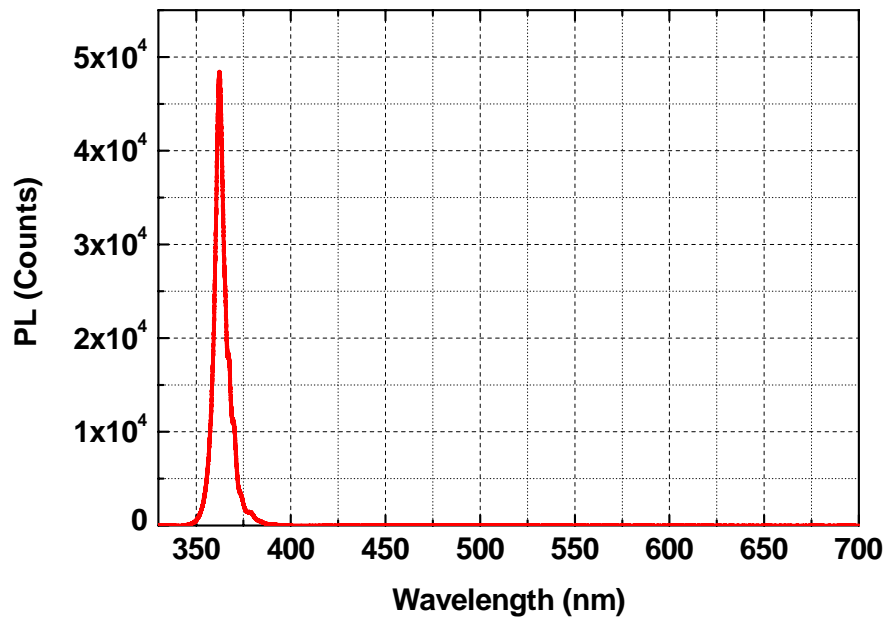


Figure 3.9: PL measurement of the UD-GaN sample.

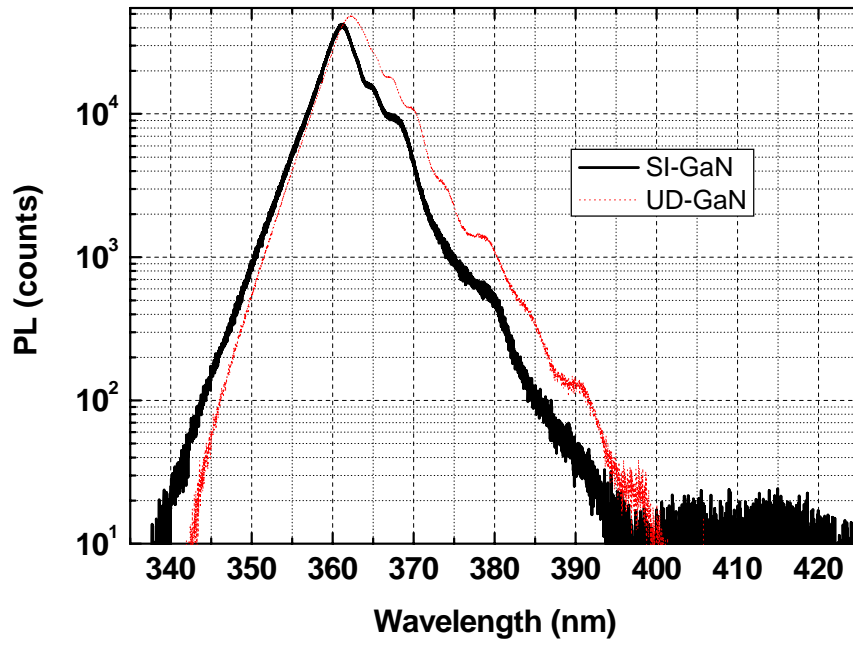


Figure 3.10: PL comparison of SI-GaN and UD-GaN templates.

Chapter 4

Fabrication

The fabrication of any microelectronic device such as our photodetectors requires a number of sequential steps. The final electrical and optical performance of the device is extremely dependent on these successive steps. Generally, these steps include ohmic/Schottky contact deposition, passivation, etching, air bridge formation, and double Bragg mirror (DBR) deposition. Unfortunately, these steps are not standard for all material systems. Each material requires its own fabrication technique. Fortunately, Metal-Semiconductor-Metal (MSM) devices have no complex fabrication steps such as DBR deposition and air bridges.

Our fabrication process consists of a standard microwave compatible with four steps adopted for an $\text{Al}_x\text{Ga}_{1-x}\text{N}$ material system. [26,28] This chapter represents these four steps in the order of fabrication. All the fabrication steps were performed in a Class-100 Clean Room at the Advanced Research Laboratory at Bilkent University.

4.1 Process Basics

In this part of the thesis, we review the basic process steps of semiconductor device fabrication that relates to our process.

4.1.1 Sample Preparation

Our MOCVD reactor can grow AlGaIn material on 2-inch sapphire substrate. It is not possible to perform fabrication on this large wafer as this would result in excessive wasting of the sample. Therefore, it is mandatory to cleave the sample in smaller pieces prior to the fabrication. Typically, one step in our photomask is approx. $6\text{ mm} \times 6\text{ mm}$. For that reason, we cut the wafers at approx. $7\text{ mm} \times 7\text{ mm}$ using a diamond dicer. We scratched the wafer on the back side with a ruler, and then fractured it by hand.

Subsequent to cleaving, we cleaned the surface of the sample. Usually there are cleaving residues and sometimes some organic dust and photoresist residues on the surface. Removing these contaminants is extremely important because they often make the device either open or short. We have two different cleaning techniques.

The first technique is used if there is not a significant amount of dirt on the sample. We put the sample in acetone for a couple of minutes. Acetone dissociates soft organic residues and it helps to remove the inorganic dirt. While the sample remains in the acetone, we gently sweep the surface with a q-tip if there is no features were previously made on the sample. Then, we put the sample in iso-propyl alcohol to remove the acetone. Finally, we put the sample under the running de-ionized (DI) water to get rid of the iso-propyl alcohol. Then, we dried the sample using a nitrogen gun. We put the sample on a hot plate at 120°C for 2 min for dehydration, when it was that the solvent cleaning was over. Afterward, we examined the sample under an optical microscope if there was any dirt left. If so, we perform this process all over again.

The second technique is used when the sample is very dirty with hard organic residues that cannot be removed by acetone. Note that this method can be used only for bare samples. If there is any deposited metal from beforehand, this method cannot be used. We used the so-called Piranha Etching technique. We prepare a solution of 3:1 $\text{H}_2\text{SO}_4:\text{H}_2\text{O}_2$. This is an extremely strong solution

for organic and metallic materials. We put our sample in this solution for 5-10 min (according to the dirt level of the sample). Then, we use DI water to clean the sample. Finally, we again use a hot plate for dehydration at 120°C for 2 min. Typically, one round is enough with this technique for cleaning the surface.

4.1.2 Photolithography

Photolithography is the most important part of the microfabrication processes. Because it is the part in which we define the features on the sample. Thus, it is required in every step. We use a polymer called photoresist, which is sensitive to UV light. By exposing with UV over a photomask we transfer the patterns on the mask to the photoresist. Then, etching and material deposition can be performed on the patterned photoresist.

We use AZ5214E image reversal photoresist, which is sensitive to 360 nm UV light and capable of patterning feature sizes $\sim 0.7 \mu\text{m}$. It can also be used as positive photoresist and is etch resistant. AZ400K developer is used to remove exposed parts of the photoresist. We utilize the Karl Suss MJB3 Mask aligner for positioning and aligning the mask.

Thereafter, the cleaning hexamethyldisilazane (HMDS) is coated on the surface in a spin coater. Then, the photoresist coating is performed. The thickness of the photoresist is related to the speed of the spinner. Every step requires its own photoresist thickness. If we aim too small, features such as $1 \mu\text{m}$, we then need thin resist. If we perform deep dry etching, then it is better to coat with thicker photoresist. Typically, we spin our photoresist at 5,000 rpm for 40 s, which corresponds to a photoresist thickness of $1.3 \mu\text{m}$. If we are performing mesa isolation etching, then we use 3,000-3,500 rpm for 40 s, which corresponds to a photoresist thickness of $\sim 1.6 \mu\text{m}$. After the spin, the samples are pre-baked at 110°C for 55 s.

There are two types of lithography such as positive and image reversal photolithography. The basic difference in these two is that in positive lithography the features on the mask are transferred in the same way to the

sample. That is, the closed (dark) features in the mask will be transferred, whereas in image reversal lithography, the patterns on the sample are reversed. That is, the open features in the mask will be transferred to the sample.

4.1.2.1 Positive Photolithography

In this method photoresist coated and pre-baked samples are exposed with an Hg lamp in the mask aligner after the alignment for approx. 40 s at 4 mW/cm², which makes 160 mJ/cm² and is enough to activate the photoresist. It is in this way that we activated the photoresist directly. Then, the samples are developed with 1:4 (AZ400K:H₂O) diluted developer for approx. 40 s. This method is used for thin metallization and etching steps.

4.1.2.2 Image Reversal Photolithography

The main difference in this method is that we expose the sample twice. First, we expose the sample for approx. 60 mJ/cm² with the mask, and then we post-bake the sample at 120°C for 120 s. Finally, we expose the sample again without the mask for 160 mJ/cm². This step is called the flood exposure. In this method the first exposure defines the features but it is insufficient to activate the photoresist. Then, when we post-bake it, the polymeric structure of the exposed photoresist changes so that after the flood exposure the opaque parts on the mask will be activated. The development part is the same as the previous method. This method is especially designated for thick metallization and small feature sized processes. Because the photoresist in our case is designed for image reversal applications, the resolution is, therefore, higher in this case.

4.1.3 Etching

Etching is one of the basic steps of microfabrication. Since devices generally utilize heteroepitaxial structures, one has to etch in order to reach deeper layers. Fortunately, MSM structures are rather simple structures. We do not have an under layer that we have to make contact with. We require the etching for two purposes only. One is the separation of the devices from one another and the other is after surface passivation, in which we need to remove

insulators from certain parts in order to make contact. There are two types of etching; dry etching and wet etching.

4.1.3.1 Dry Etching

There are a number of techniques used for dry etching in semiconductor device fabrication technology. Reactive Ion Etching (RIE), plasma etching, Ion milling are examples of dry etching techniques. In our lab, we use a RIE facility that etches the surface by accelerating reactive ion plasma in a low pressure environment. The ions remove the surface atoms by chemical reaction or simply by physical collision. For etching AlGaIn and GaIn materials we used CCl_2F_2 gas as an etchant. Etch rates differed from 20 nm/min to 45 nm/min for AlGaIn and GaIn.

4.1.3.2 Wet Etching

Wet etching was the first etching technique to ever be used in semiconductor science. It is based on chemical reactions between the substrate surface and the etchant solution. When a substrate is put in its etchant solution, the reaction initiates and eventually the substrate is removed from the surface. We use wet etch to etch SiN_x which we deposit on top of the surface for passivation. In order to etch SiN_x we use 1:100 dilute HF solution. Etch rate is typically 30 nm/s.

4.1.4 Deposition

It is not possible to grow all the layers as needed via epitaxy. One has to deposit additional material such as metals for contacts and dielectrics for electrical isolation or optical components such as mirrors, waveguides etc. In our process, we deposit metals for contacts and SiN_x for surface passivation and antireflection coating purposes.

4.1.4.1 Metallization

We deposit metals on the samples for different purposes. In the case of MSM photodiodes, we need two kinds of metallization such as Schottky contact formation and interconnect metallization.

We have an ultra high vacuum (UHV) LE590 box coater for metal depositions. It is a thermal evaporator. Metals are placed in tungsten boats. Then, they are evaporated by running a high electrical current through these tungsten resistors in UHV. The deposited metal thickness is monitored throughout the process via detectors. Therefore, we can precisely adjust and monitor the deposited metal thickness.

4.1.4.2 Dielectric Coating

All the dielectric coating steps are performed in a Plasma Enhanced Chemical Vapor Deposition (PECVD) system in our laboratory. The system uses different gases as the reaction precursors. For SiN_x coating, we use silane (2% SiH_4 +98% N_2) as the Si source and ammonia (NH_3) as the N source. We have a vacuum chamber in which we create plasma of silane and an ammonia mixture. The flow rates of each gas are crucial for the composition of the deposited material. The ions of plasma are accelerated towards the sample surface, which is heated to 250°C . Then, the reaction occurs. Si and N atoms are deposited as SiN_x and the rest is taken out through exhaust.

4.2 Device Fabrication Steps

We fabricated our devices using microwave compatible four steps. These steps are mesa isolation, Schottky contact formation, dielectric coating, and interconnect metallization.

4.2.1 Mesa Isolation

The mesa isolation step is, in essence, the removal of the connection between the devices. By this step the device active areas were defined, and were

isolated from one another. Unfortunately, AlGaIn material is one of the hardest materials. The etch rate is extremely low and moreover it is comparable to the etch rate of the photoresist. Therefore, this step causes many problems during the process. Generally, mesa isolation is one of the last steps with other materials. We on the other hand changed the sequence and started the process with mesa isolation. We generally perform this step twice because photoresist is insufficiently strong to hold all the way down to the sapphire. After this step, there are semiconductor islands left only on sapphire. (See figure 4.1)

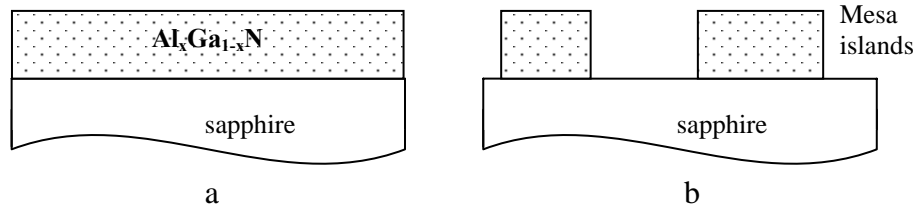


Figure 4.1: Sample before (a) and after (b) mesa isolation step.

4.2.2 Schottky Contact Formation

This is the most important part of our process because all the physics occurred under these contacts. According to our device geometry, these Schottky contacts are in the form of two separate interdigitated fingers. Because of that, this step is also called finger metallization. The finger width and pitch are in the range of $1\ \mu\text{m}$ to $20\ \mu\text{m}$. We used Ni and Au for finger metallization. The coated metal thicknesses were $3\ \text{nm}$ for Ni and $6\ \text{nm}$ for Au. As you can observe, we coat very thin metal in this step. This is because we want our metal to be as transparent to UV light as possible. Normally half of the surface was covered with metal already. Therefore, if we coat with thick metal, then only half of the incident light will be able to enter the device. We deposit thin metal to avoid that situation. (See figure 4.2)

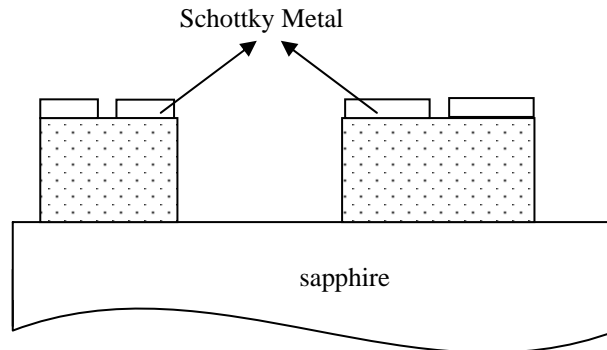


Figure 4.2: Schottky metallization

4.2.3 Dielectric Coating

This step produces a protective layer on top for finger metals from outside effects as well as it serves as an antireflection layer. We determined the thickness of the SiN_x layer as follows. The layer thickness should be $\lambda/2n$ in order to minimize the reflection for a specific wavelength λ , where n is the refractive index of silicon nitride. We used PECVD to coat the dielectric on the sample. PECVD coats the surface to where the walls of the mesa island are also coated along with the top surface. (See figure 4.3) This property helps us to prevent interconnect metals from touching the semiconductor material. After the deposition, we etch the required parts of the SiN_x layer through the openings of photoresist with an $\text{HF}:\text{H}_2\text{O}$ (1:100) solution.

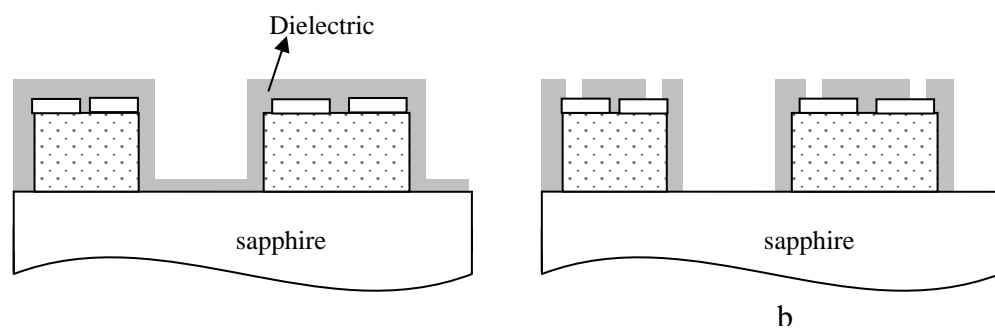


Figure 4.3: (a) Sample surface after dielectric coating, (b) Sample surface after wet etching with HF.

4.2.4 Interconnect Metallization

This is the final step of the device fabrication. The Schottky metal area is very small, and the metal is very delicate. Therefore, we need to make larger and thicker contact pads to be able to test our devices. Interconnect pads have main contacts that are used to touching the two separate Schottky metals. In addition, there are two microwave compatible transmission lines surrounding the device. We again, thermally evaporated the metal for this step as 50 nm Ti and 700 nm Au. Notice that this is a very thick metal, and therefore, we used image reversal photolithography in this step. The main role of Ti here is to make the gold stick to the sapphire surface. See (figure 4.4)

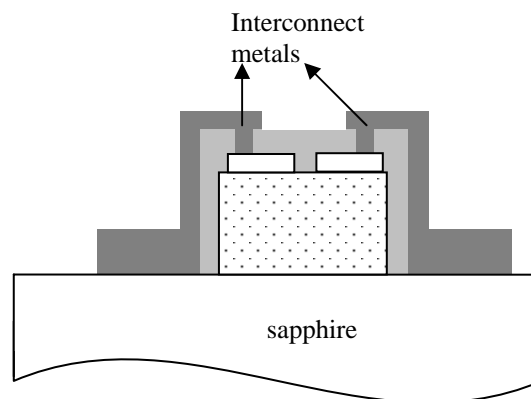


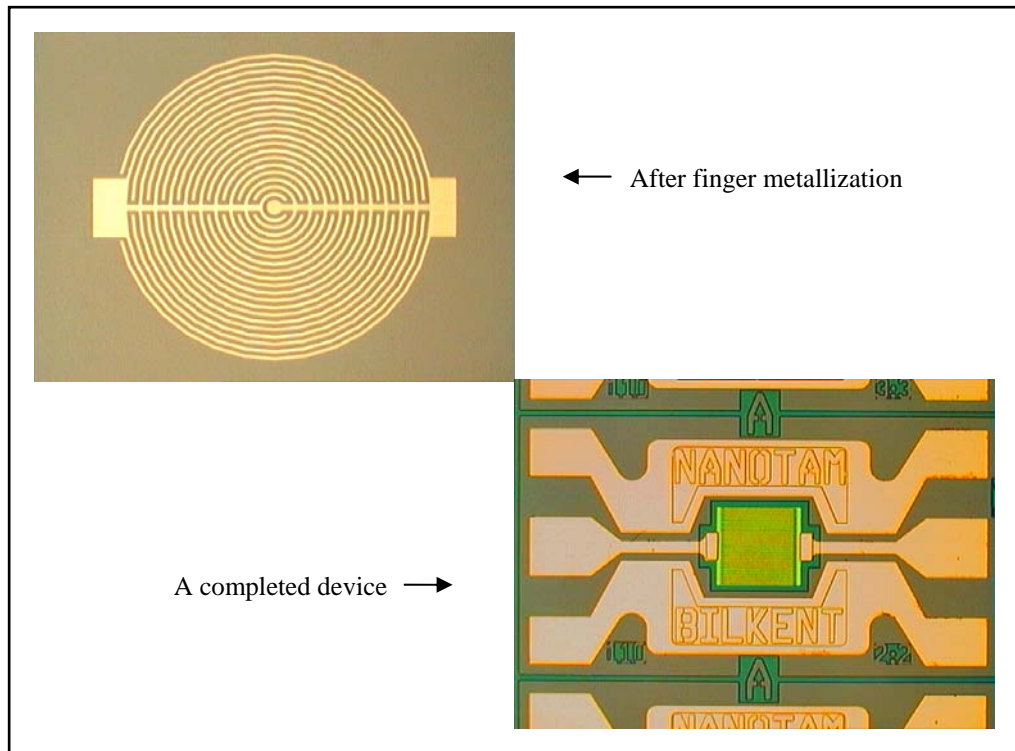
Figure 4.4: Finalized device.

4.2.5 Lift Off

All the steps involving metallization has a process called lift off. It is the part in which we get rid of the excess metal part coated during thermal evaporation. We placed the sample in acetone. Acetone dissolves photoresist immediately and the metal on the photoresist is lifted off. Sometimes some light agitation is enough for the lift off of the metal, especially in the finger metallization step because the metal is very thin. However, the steps such as in interconnect metallization require more vigorous methods such as ultrasound or even sweeping the sample with a Q-tip.

Step	Parameters
Mesa isolation etch	Photolithography: positive Spin: 3500 rpm Etchant: CCl_2F_2 Pressure: 8 mbar Gas flow: 20 sccm RF power: 100 W
Finger metallization	Photolithography: positive Spin: 6000 Metals: Ni/Au Thickness: 3 nm/6 nm
Silicon nitride deposition	Silane flow: 180 sccm Ammonia flow: 45 sccm RF power: 20 W Pressure: 1000 mTorr Temp: 250°C Thickness: 250 nm
Silicon Nitride Etch	Photolithography: positive Spin: 5000 Etchant: 1:100 HF:H ₂ O Time: ~7 sec.
Interconnect Metallization	Photolithography: positive Spin: 5000 Metals: Ti/Au Thickness: 50 nm/700 nm

Table 4.1: Technical data sheet of the MSM photodetector fabrication



Figur 4.5: Micrographs taken during the fabrication

Chapter 5

Measurements

This chapter represents our experimental results from the fabricated devices. We fabricated three different wafers. The first detector sample had a low cut-off wavelength and high UV-visible rejection ratio and was fabricated from the $\text{Al}_{0.75}\text{Ga}_{0.25}\text{N}$ wafer. This photodetector is called a Deep-UV photodetector. The second detector sample was fabricated from an SI-GaN sample and its advantage was the lowering of dark current. Finally, the third detector sample was made on a regular UD-GaN wafer, which was used as a reference for comparison with the detector sample two. These two samples are called Visible Blind Photodetectors.

We performed current-voltage (IV), quantum efficiency (QE), responsivity upon low incident optical power and noise measurements on the fabricated devices. We will present these results as two separate chapters. The first chapter will be about detector sample one and the second chapter will be about detector sample two and three.

5.1 Experimental Results of the Deep-UV Photodetectors

5.1.1 Current vs. Voltage Characteristics

Current-Voltage (IV) characteristics were carried out using a Keithley 6517A high resistance electrometer with low noise triaxial cables in a grounded

shielded Faraday cage. Since we were measuring MSM photodiodes, the IV characteristics did not have a diodic character exactly. This is because the structure has two diodes connected back to back so that, normally, the current cannot pass through in each direction. The resulting devices exhibited extremely low dark currents and very high breakdown voltages. Figure 5.1 shows the I-V curve of a $4\ \mu\text{m}$ finger width/spacing device. As you can see, the dark current level is below 100 fA up to $\pm 100\text{V}$ bias voltage (see figure 5.2). This dark current value corresponds to $5.8 \times 10^{-10}\ \text{A}/\text{cm}^2$ dark current density under 50 V bias given the device area of $100 \times 100\ \mu\text{m}^2$. We increased the bias voltages up to 350 V and even under this high bias voltage level, dark current does not exceed 100 pA. The curve in the figure 5.1 indicates a sign of soft breakdown when the bias voltage approaches 300 V. These low dark current and high breakdown voltage values were good signs of the high quality of our $\text{Al}_{0.75}\text{Ga}_{0.25}\text{N}$ epitaxial layer.

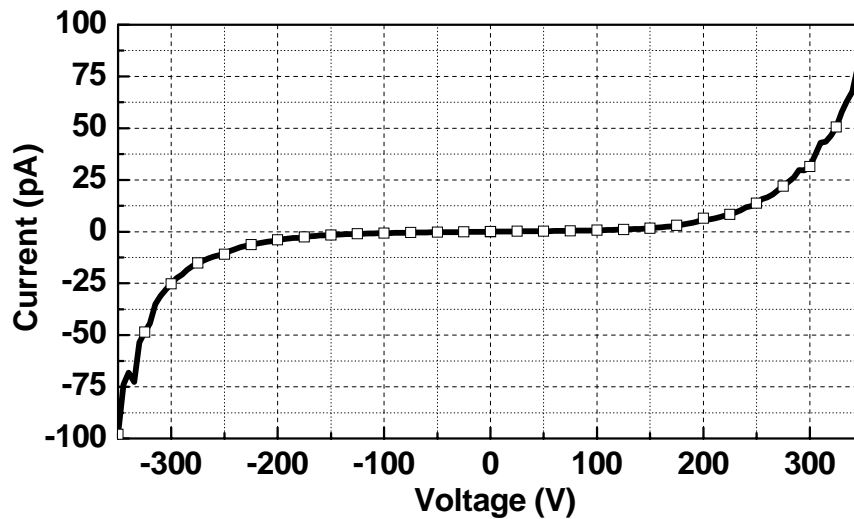


Figure 5.1: IV Characteristics of a $100 \times 100\ \mu\text{m}^2$ area device.

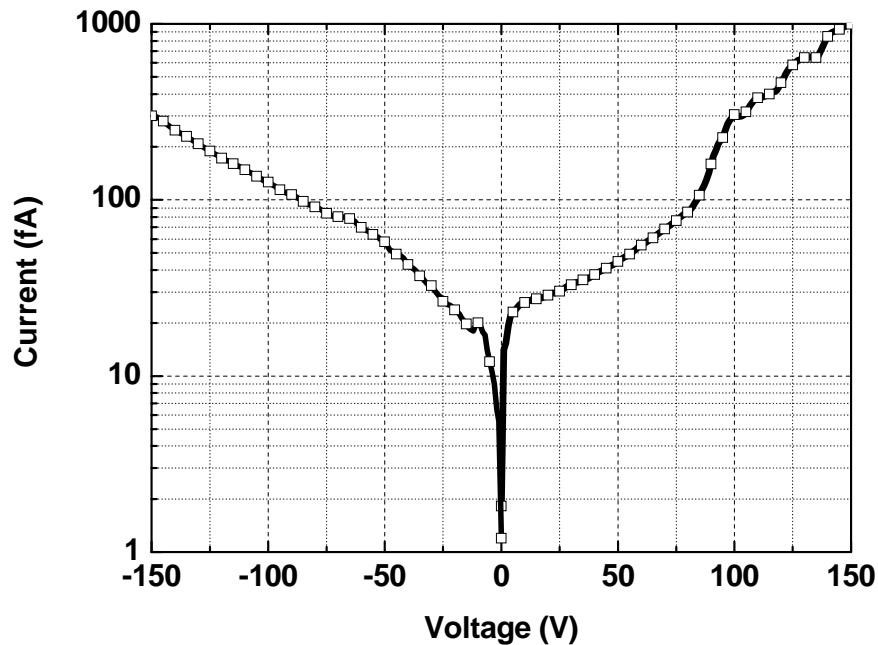


Figure 5.2: IV Characteristics of a 4 μm finger width/spacing and $100 \times 100 \mu\text{m}^2$ area device in a semilog scale.

5.1.2 Quantum efficiency/Responsivity Measurements

The spectral responsivity measurements were performed in a range of 200 – 400 nm using an Xe lamp, a monochromator, and a calibrated Si photodetector. We recorded the photocurrent using a Keithley 6517A electrometer. You can see the experimental setup in figure 5.3. The continuous output of the Xe lamp passes through a computer controlled monochromator to produce a single wavelength output. The output of the monochromator is sent to the photodetector by a fiber and a fiber micropositioner, which is mounted on the probe station. The electrical connection of our photodetectors is again performed by micropositioners and low noise DC probes. We apply a DC bias with the voltage source of the electrometer and read the current with an ammeter of the electrometer. Prior to the experiment we recorded the optical power output of the Xe lamp and monochromator system with a calibrated Si photodetector. We placed a Si photodetector exactly where we put our own

photodetector, and then we recorded the optical power. We repeated this part every time before we started a measurement.

The resulting responsivity curves as a function of applied bias voltage of a $400 \times 400 \mu\text{m}$ device with $2 \mu\text{m} / 3 \mu\text{m}$ finger width/spacing, which are shown in figure 5.4. Devices exhibited a sharp cut off at 229 nm and a peak photoresponse at 222 nm, which was in good agreement with the transmission measurements (see figure 3.3). Device responsivity increased with applied voltage and reached 0.53 A/W at a 50 V bias voltage under 222 nm UV illumination, which corresponds to a quantum efficiency higher than 250%. This situation can be explained by the photoconductive gain in MSM structures.

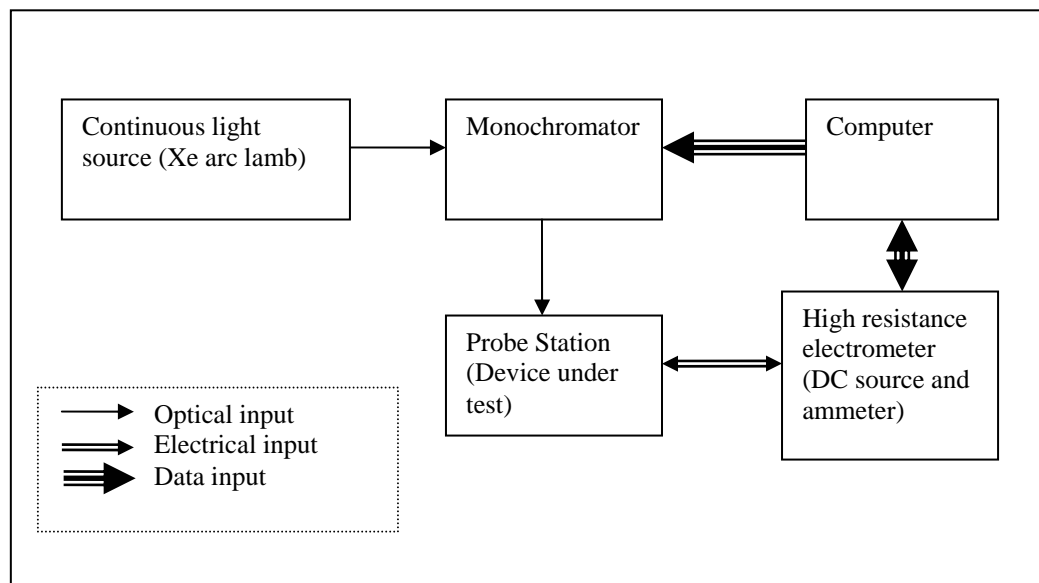


Figure 5.3: Schematic diagram of our Quantum efficiency setup.

Figure 5.4 also points out the fact that UV/VIS rejection ratio reached seven orders of magnitude at a 20 V bias voltage at 400 nm wavelength. This rejection ratio was the best result reported in the literature for AlGaN based MSM photodetectors.

We also made a calculation for the detectivity of our photodetectors using a thermally limited detectivity (D^*) formula (see equation 2.16). We found a detectivity of $1.64 \times 10^{12} \text{ cmHz}^{1/2}/\text{W}$ at 222 nm, which corresponds to a noise equivalent power (NEP) $7.87 \times 10^{-15} \text{ W/Hz}^{1/2}$ at room temperature.

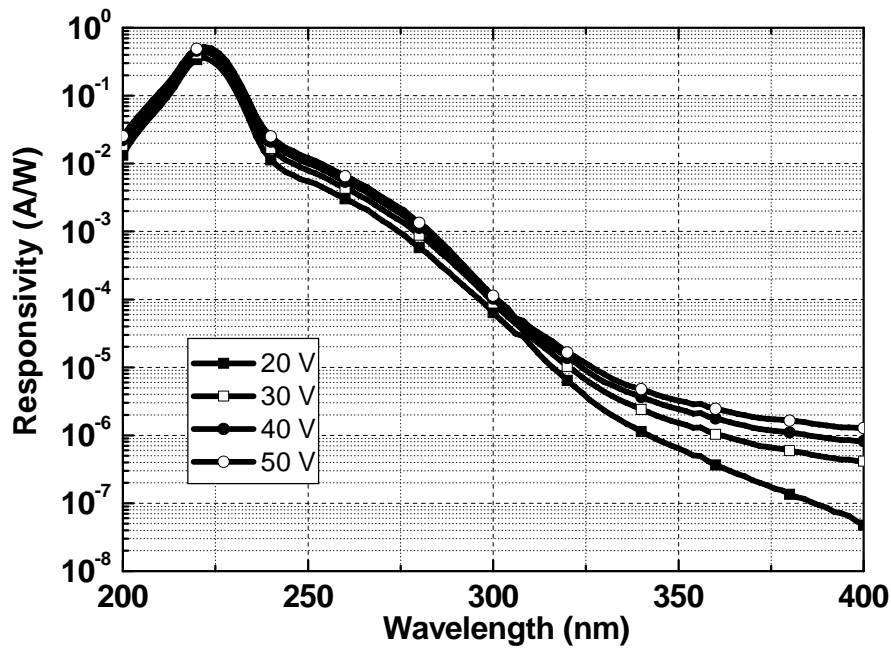


Figure 5.4: Spectral responsivity measurements of a $400 \times 400 \mu\text{m}$ photodetector.

5.1.3 Noise Characterization

The final measurement performed on Deep-UV photodetectors was the spectral noise measurement. We were aiming to determine the dominant noise mechanism in these detectors. As you can follow from figure 5.5, our setup consists of a fast Fourier transform (FFT) spectrum analyzer, current amplifier, DC voltage source, and a microwave probe station. $3 \times 10^{-29} \text{ A}^2/\text{Hz}$ was our setup noise floor for frequencies higher than 1 kHz and increased at lower frequencies. We had to investigate devices with relatively high leakage currents

because most of our detectors exhibited noise densities well below the noise floor.

Figure 5.6 shows the low frequency spectral noise density ($S_n(f)$) of a $100 \times 100 \mu\text{m}^2$ device at 0 V, 25 V, and 50 V bias.

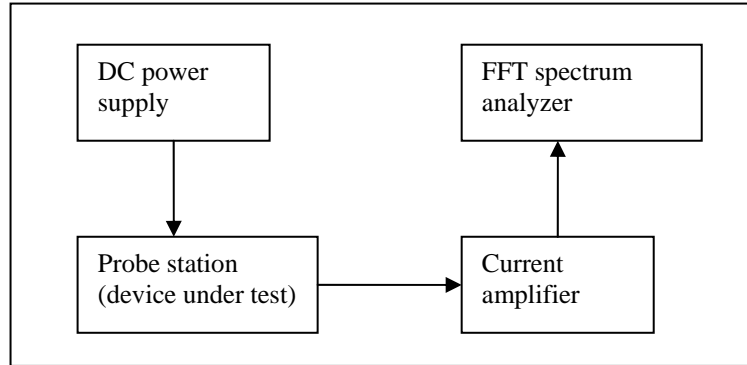


Figure 5.5: Experimental setup for noise measurements.

$S_n(f)$ values are $8.88 \times 10^{-29} \text{ A}^2/\text{Hz}$, $1.44 \times 10^{-27} \text{ A}^2/\text{Hz}$, and $8.36 \times 10^{-26} \text{ A}^2/\text{Hz}$ at 0 V, 25 V, and 50 V bias voltages respectively at 1 Hz. According to the behavior of the noise curves, $1/f$ (flicker) is the dominant noise mechanism, which is typical for Schottky barrier $\text{Al}_x\text{Ga}_{1-x}\text{N}$ detectors at low frequencies. Furthermore, the noise curves obey the relation $S_n = S_0/f^\gamma$ with the fitting parameter γ varying from 1.1 to 1.2. The noise and the detectivity performance of our devices indicate that our MSM photodetectors are suitable for low-noise applications.

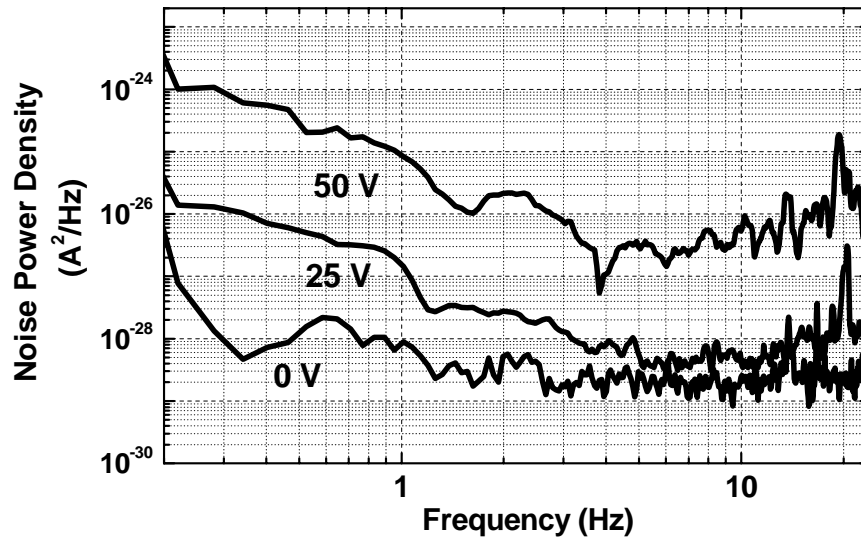


Figure 5.6: Spectral noise measurement of a high-leakage $100 \times 100 \mu\text{m}$ photodetector with a varying applied bias voltage.

5.2 Experimental Results of the Visible Blind Photodetectors

5.2.1 Current vs. Voltage Characteristics

The IV measurements of the two GaN visible blind samples were performed in the same manner as the Deep-UV sample. The devices fabricated on the SI-GaN sample exhibited extremely low dark current values, while those fabricated on the UD-GaN sample exhibited higher dark current values. The dark current level measured of UD-GaN is typical for such devices reported previously. There was no significant breakdown voltage difference between these two devices. The breakdown level was observed at bias voltages as high as 200 V for $200 \times 200 \mu\text{m}$ active area detectors fabricated on both SI-GaN and UD-GaN samples. Figure 5.7 compares the dark I-V curves of $10 \mu\text{m}$ finger width/spacing devices from the two separate samples. The dark current measured from devices fabricated on the SI-GaN chip remains below 1 pA and up to 100 V bias voltage, whereas the dark current is approx. 100 nA at 100 V

bias. In terms of the dark current density; the dark current density (at 50 V bias) of a device fabricated on the SI-GaN chip is calculated as 1.96×10^{-10} A/cm². In comparison, the 50 V dark current density calculated for a similar device fabricated on UD-GaN is 8.1×10^{-6} A/cm², which corresponds to four orders of magnitude improvement.

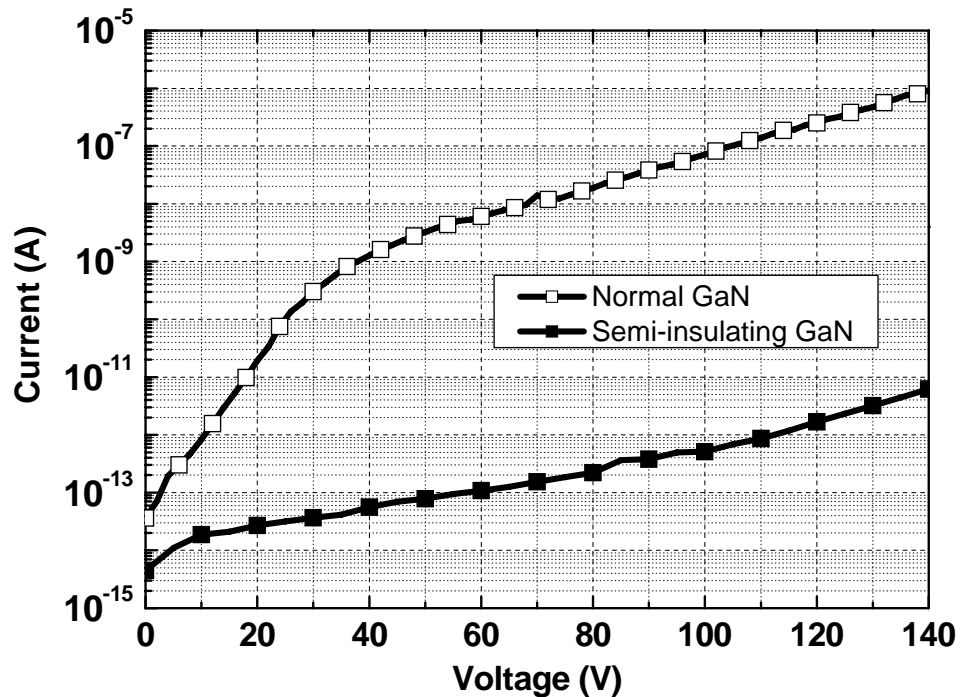


Figure 5.7: Current-voltage characteristics of $200 \times 200 \mu\text{m}$ MSM photodiodes with $10 \mu\text{m}/10 \mu\text{m}$ finger width/spacing on two different chips.

5.2.2 Responsivity Measurements

Spectral responsivity measurements of both samples were performed in the range of 250-450 nm using a Xe arc lamp, a monochromator, and a calibrated Si photodetector, which is calibrated through a range of 190-1100 nm. The photocurrent was measured in two different ways: The DC (unmodulated) photocurrent was measured in the same manner as the Deep-UV photodetector. We used a high resistance electrometer to record the photocurrent (see figure 5.3

for details). The AC (modulated) photocurrent, however, was recorded by a lock-in amplifier using an optical chopper to modulate the monochromator output illustrated in figure 5.8.

Figure 5.9 and 5.10 illustrate unmodulated responsivity curves as a function of applied bias voltage for $200 \times 200 \mu\text{m}$ devices with $3 \mu\text{m}/3 \mu\text{m}$ finger width/spacing on UD-GaN and SI-GaN samples, respectively. Devices on both chips exhibited a sharp cut off at 365 nm, while the peak of the photoresponse was observed at 360 nm. These cut off and peak responsivity values are in very good agreement with PL measurements shown in figure 3.10. Device responsivity increased with applied voltage and reached 101.80 A/W for SI-GaN and 88.63 A/W for UD-GaN at 50 V bias and 365 nm UV illumination. These very high responsivity values indicate that devices have a gain of approx. 700, which can be attributed to the photoconductive gain mechanism in MSM detectors.

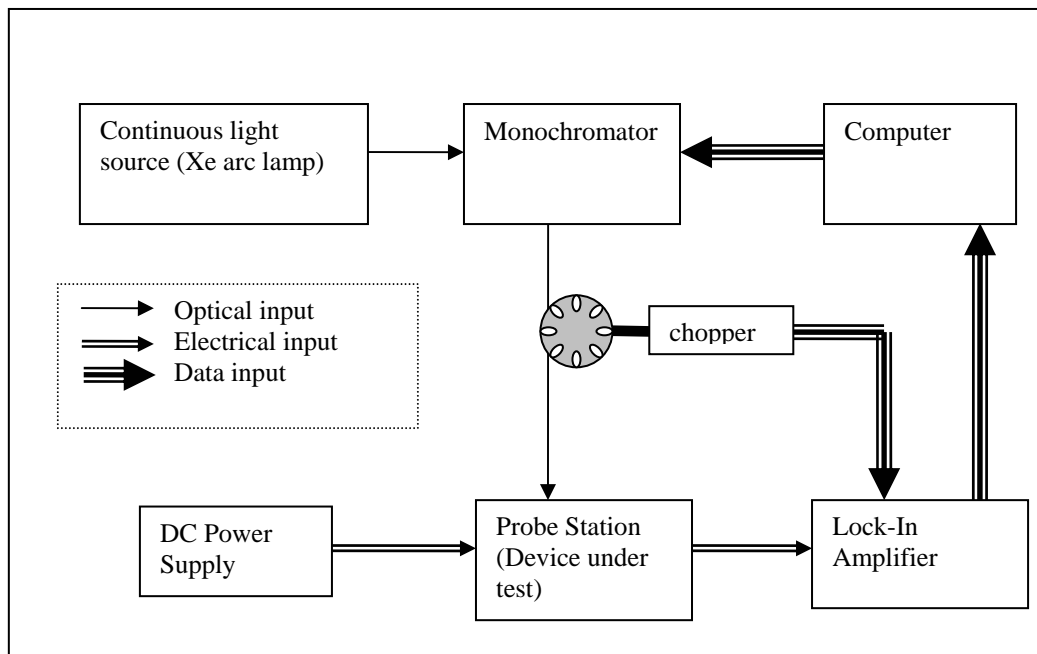


Figure 5.8: Schematic diagram for a modulated spectral responsivity measurement.

Using a thermally limited detectivity (D^*) formula (see equation 2.16) we find a detectivity of 1.3×10^{14} $\text{cmHz}^{1/2}/\text{W}$ and 1.2×10^{13} $\text{cmHz}^{1/2}/\text{W}$ at 360 nm at 0 V bias for SI-GaN and UD-GaN chips, respectively. Detectivity of the SI-GaN sample reached 3.12×10^{17} $\text{cmHz}^{1/2}/\text{W}$ at 50 V bias. These detectivity values are the best results reported in the literature for a GaN based MSM photodiode. These high detectivity values are even comparable with that of photomultiplier tubes and AlGaIn based photodetectors [29-31]. Although there is no significant difference in terms of responsivity in these two devices, there is a significant improvement in terms of detectivity. This is obvious because of the high differential resistance of the SI-GaN sample.

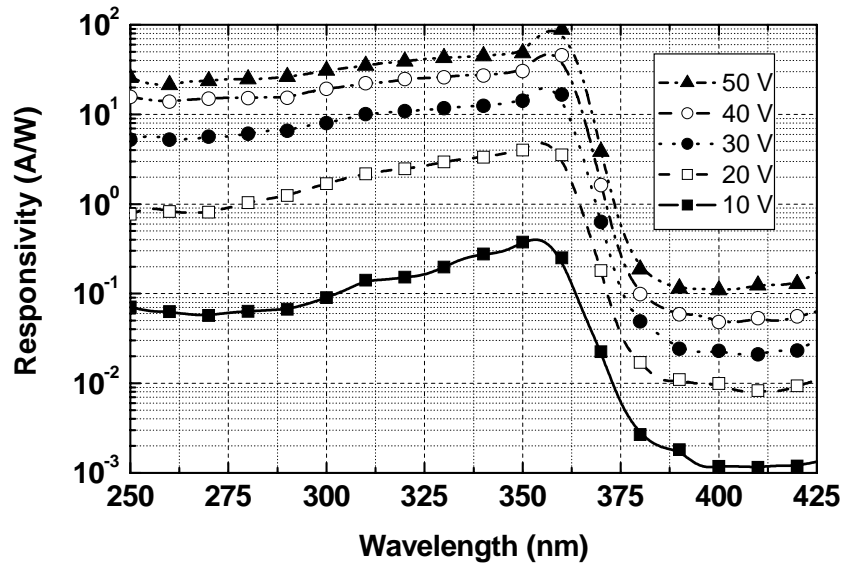


Figure 5.9: Measured spectral responsivity curves of $200 \times 200 \mu\text{m}$ devices with $3 \mu\text{m}/3 \mu\text{m}$ finger width/spacing on the UD-GaN sample.

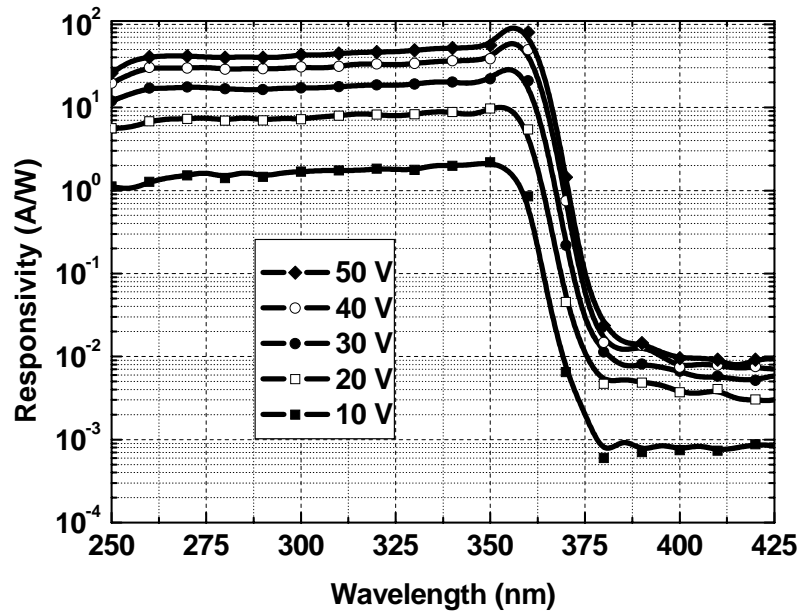


Figure 5.10: Measured spectral responsivity curves of $200 \times 200 \mu\text{m}$ devices with $3 \mu\text{m}/3 \mu\text{m}$ finger width/spacing on the SI-GaN sample.

The modulated photoresponse measurements of the photodetector on the SI-GaN sample as a function of the bias voltage are represented in figure 5.11. The aim was to investigate the dependence of the gain on the modulation frequency. Normally, we expect a small decrease in responsivity [13]. As illustrated in the figure 5.11 the device responsivity decreases with the chopper frequency as was expected. However, there is a significant gain is observed even at the setup high frequency limit of 400 Hz.

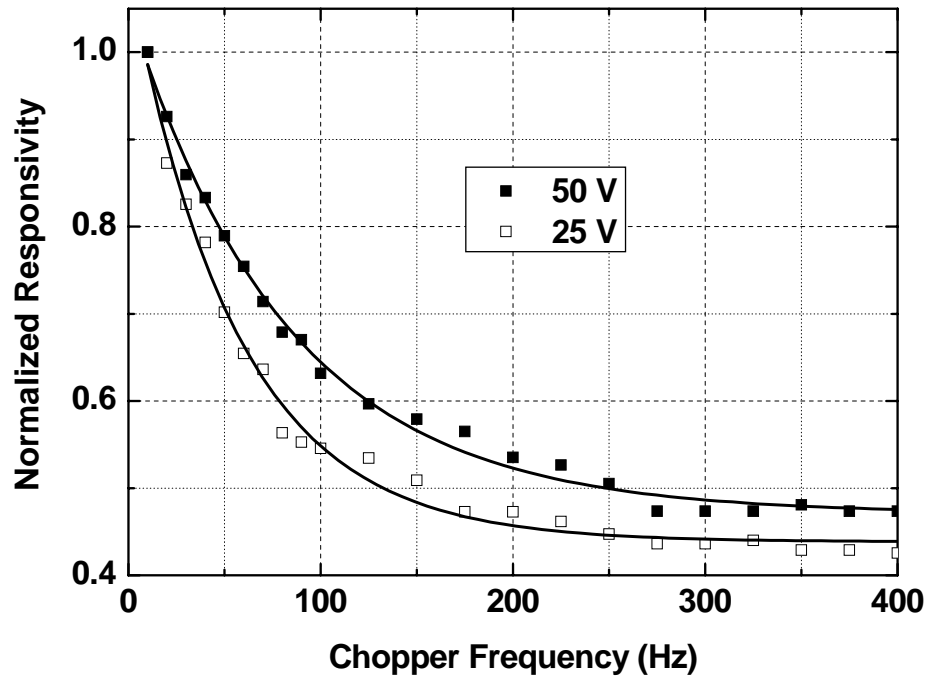


Figure 5.11: Normalized modulated photoresponse of a $200 \times 200 \mu\text{m}$ device with $3 \mu\text{m}/3 \mu\text{m}$ finger width/spacing on the SI-GaN chip as a function of chopper frequency.

5.2.3 Low Power Photodetection

Since the detectivity values of our photodetector measured this much higher, we investigated the device performance under low optical powers. Low optical power responsivity measurement was performed by using a series of neutral density filters to vary the incident optical power in the few pW to 1 nW range. As expected, very low level signals are detectable because of the high sensitivity due to high gain and low dark current values. As shown in figure 5.12, the measured DC photocurrent is well above the dark current at the corresponding bias voltage even for incident optical powers as low as 3 pW.

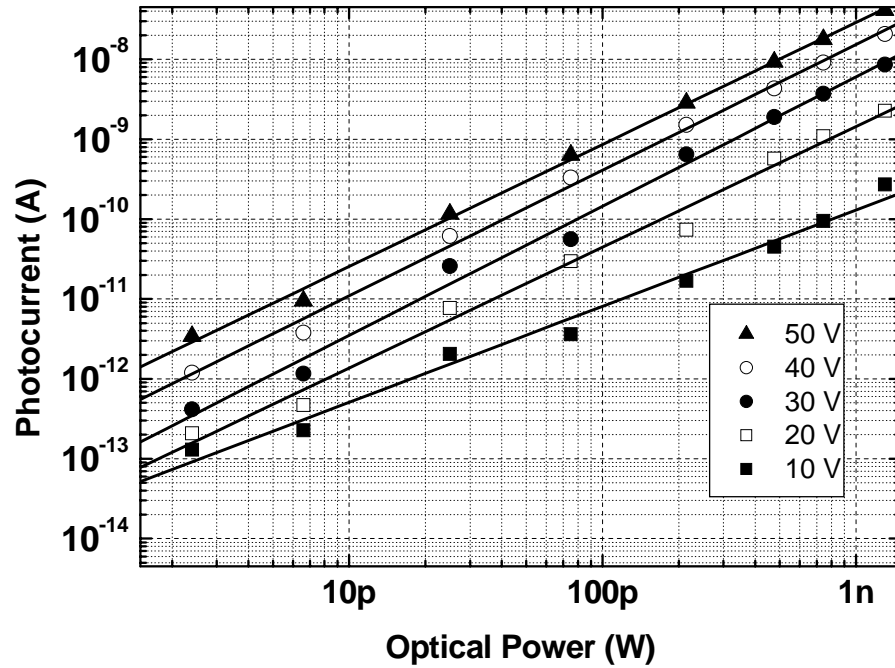


Figure 5.12: Measured photocurrent of a $200 \times 200 \mu\text{m}$ device with $3 \mu\text{m}/3 \mu\text{m}$ finger width/spacing on the SI-GaN chip as a function of optical power and bias voltage. The dashed lines represent the linear fits to the plotted data.

Chapter 6

Achievements and Future Directions

In the preceding chapters we presented the growth process of $\text{Al}_{0.75}\text{Ga}_{0.25}\text{N}$ and SI-GaN materials on sapphire substrates using Metalorganic Chemical Vapor Deposition (MOCVD). We also grew one regular GaN sample for comparison. After that, the fabrication of metal semiconductor metal (MSM) photodiodes on these three samples was presented. We developed our own fabrication technique and sequence during these processes.

The fabricated Deep-UV MSM photodetector has a cut off wavelength of $\lambda_c = 229$ nm, which was the lowest cut off wavelength reported for a AlGaN based MSM photodiode. The devices have shown a responsivity of 0.53 A/W under 50 V bias and a detectivity of 1.64×10^{12} $\text{cmHz}^{1/2}/\text{W}$ under 222 nm UV light illumination. A leakage current density of 5.79×10^{-10} A/cm^2 at 50 V bias voltage was obtained from the fabricated MSM photodetectors. They have noise density as low as 8.36×10^{-26} A^2/Hz at 50V and 1 Hz. Noise curves obey the $S_n = S_0/f^\gamma$ relation showing that 1/f (flicker) noise is the dominant noise mechanism. We achieved a UV/VIS rejection ratio of seven orders of magnitude, which is a record value for an MSM structure reported in the literature to date.

In addition, we fabricated tested visible blind MSM photodiodes on SI-GaN templates. We also made a comparison of these devices with identical ones fabricated on a regular UD-GaN control sample. Devices on the SI-GaN chip exhibited a dark current density of 1.96×10^{-10} A/cm² at 50 V bias voltage, which is four orders of magnitude lower compared with the devices on the UD-GaN chip. No sign of device breakdown was observed at bias voltages as high as 200 V for both samples. For 360 nm UV illumination and at a 50 V bias, responsivity values as high as 101.8 A/W and 88.63 A/W were obtained from the SI- and UD-GaN samples, respectively. The photoresponse of both samples was comparable with no significant difference. All of the devices exhibited a relatively flat response in the 250-360 nm range with a sharp cut-off at 365 nm. The low power photodetection measurements show that MSM photodetectors fabricated on SI-GaN templates can detect low level optical signals on the order of a few pW because of high internal gain and low dark current.

For future work, our plan is to investigate the mechanism of the high internal gain. It might be possible to realize this high internal gain as in GaN for AlGaIn material. The goal is to come up with a simple MSM structure instead of complex avalanche photodiodes for applications such as photon counting. Lastly, future research should utilize the same idea of SI-GaN for AlGaIn in order to make it more resistive to where the sensitivity of the devices on these templates will be higher.

Bibliography

- [1] I. Akasaki, H. Amano, K. Itoh, N. Koide, and K. Manabe, "GaN Based UV/Blue light emitting devices" *Inst. Phys. Conf. Ser.* **129**, 851 (1992).
- [2] T. Mukai, M. Yamada, and S. Nakamura. "Current and temperature dependence of electroluminescence of InGaN based UV/blue/green light emitting diodes" *Jpn. J. Appl. Phys.* **37**, L1358 (1998).
- [3] T. Nishida, and N. Kobayashi, "346 nm emission from AlGaN multi quantum well light emitting diodes" *Phys Stat. Sol. A.* **176**, 45 (1999).
- [4] P. Schreiber, T. Dang, G. Smith, T. Pickenpaugh, P. Gehred, and C. Litton, "Solar Blind UV region and UV detector development objectives", *Proc. SPIE*, vol 3629, 230, (1999).
- [5] Y.D. Jhou, C.H. Chen, S.J. Chang, Y.K. Su, P.C. Chang, P.C. Chen, H. Hung, C.L. Yu, S.M. Wang and M.H. Wu, *Microelectron. J.* **37** (4): 328-331 (2006).
- [6] M. S. Shur and A. Zukauskas, *UV Solid-State Light Emitters and Detectors*, Kluwer Academic, Dordrecht, 2003.

- [7] M. Razeghi and A. Rogalski, "Semiconductor ultraviolet detectors" *J. Appl. Phys.* **79**,7433, (1996).
- [8] H. Markoc, *Nitride semiconductors and devices*, Springer Verlag, Germany, (1992).
- [9] D. Walker,X. Zhang,P. Kung,A. Saxler,S. Javapour,J. Xu, and M. Razeghi, "AlGa_N ultraviolet photoconductors grown on sapphire" *Appl. Phys. Lett.*, **68**, 2100 (1996)
- [10] B. W. Lim,Q.C. Chen, J. Y. Yang, M. Asif Khan, "High responsivity intrinsic photoconductors based on Al_xGa_{1-x}N" *Appl Phys Lett*, **68**, 3761 (1996)
- [11] A. Osinsky, S. Gangopadhyay, B. W. Lim, M. Z. Anwar, M. A. Khan, D. V. Kuksenkov and H. Temkin, "Schottky barrier photodetectors based on AlGa_N" *Appl. Phys. Lett.* **72**, 742 (1998).
- [12] T. Tut, N. Biyikli, I. Kimukin, T. Kartaloglu, O. Aytur, M. S. Unlu and E. Ozbay, "High bandwidth-efficiency solar-blind AlGa_N Schottky photodiodes with low dark current" *Solid State Electronics.* **49**, 117 (2005).
- [13] U. Chowdhury, M. M. Wong, C. J. Collins, B. Yang, J. C. Denyszyn, J. C. Campbell and D. Dupuis, "High-performance solar-blind photodetector using an Al_{0.6}Ga_{0.4}N n-type window layer" *J. Cryst. Growth.* **248**, 552 (2003).
- [14] C. J. Collins, U. Chowdhury, M. M. Wong, B. Yang, A. L. Beck, R. D. Dupuis, and J. C. Campbell, "Improved solar-blind detectivity using an Al_xGa_{1-x}N heterojunction *p-i-n* photodiode" *Appl. Phys. Lett.*, **80**, 3754 (2002)
- [15] M.M. Wong, U. Chowdhury, C.J. Collins, B. Yang, J.C. Denyszyn, K.S. Kim, J.C. Campbell, R.D. Dupuis, "High Quantum Efficiency

- AlGaIn/GaN Solar-Blind Photodetectors Grown by Metalorganic Chemical Vapor Deposition” *Phys. Status Solidi A*, **188**, 333 (2001)
- [16] T. Li, D. J. H. Lambert, A. L. Beck, C. J. Collins, B. Yang, J. M. M. Wong, U. Chowdhury, R.D. Dupuis and J. C. Campbell, “Solar-blind $\text{Al}_x\text{Ga}_{1-x}\text{N}$ -based metal-semiconductor-metal ultraviolet photodetectors” *Electron. Lett.* **36**, 1581 (2000).
- [17] N. Biyikli, I. Kimukin, T. Kartaloglu, O. Aytur, and E. Ozbay, “High-speed solar-blind AlGaIn-based metal–semiconductor–metal photodetectors” *Phys. Status Solidi C*, **7**, 2314 (2003).
- [18] J. Y. Duboz, J. L. Reverchon, D. Adam, B. Damilano, N. Grandjean, F. Semond, and J. Massies, “Submicron metal–semiconductor–metal ultraviolet detectors based on AlGaIn grown on silicon: Results and simulation” *J. Appl. Phys.*, **92**, 5602 (2002).
- [19] N. Biyikli, I. Kimukin, T. Tut, O. Aytur, and E. Ozbay, *Electronic Letters*, “Fabrication and characterization of solar-blind $\text{Al}_{0.6}\text{Ga}_{0.4}\text{N}$ MSM photodetectors” **41**, 276 (2005).
- [20] D. Walker, V. Kumar, K. Mi, P. Sandvik, P. Kung, X. H. Zhang, and M. Razeghi, “Solar-blind AlGaIn photodiodes with very low cutoff wavelength” *Appl. Phys. Lett.*, **76**, 403 (2000).
- [21] E. Monroy, T. Palacios, O. Hainaut, F. Omnes, F. Calle, JF. Hochedez, “Assessment of GaN metal–semiconductor–metal photodiodes for high-energy ultraviolet photodetection” *Appl. Phys. Lett.* **80**, 3198 (2002).
- [22] S. Donati, *Photodetectors: devices, circuits, and applications*, Prentice Hall, Upper Saddle River, NJ, 2000.
- [23] S. L. Chuang, *Physics of Optoelectronic Devices*, Wiley, New York, 1995.

- [24] S. M. Sze. *Physics of Semiconductor Devices*, Wiley, New York, 1981.
- [25] S. R. Lee, A. F. Wright, M. H. Crawford, G. A. Petersen, J. Han and R. M. Biefeld, "The band-gap bowing of $\text{Al}_x\text{Ga}_{1-x}\text{N}$ alloys" *Appl. Phys. Lett.* **74** 3344 (1999).
- [26] N. Biyikli, High Performance $\text{Al}_x\text{Ga}_{1-x}\text{N}$ Based UV Photodetectors for Visible/Solar Blind Applications, Bilkent University Ph. D. Thesis, May 2004.
- [27] M. Razeghi, *The MOCVD Challenge Volume 2: A Survey of GaInAsP-GaAs for Photonic and Electronic Device Applications*, IOP Publishing, Bristol, 1989.
- [28] T. Tut, $\text{Al}_x\text{Ga}_{1-x}\text{N}$ Based Solar Blind Schottky Photodiodes, Bilkent University M.S. Thesis, January 2004.
- [29] J. D. Brown, Z. Yu, J. Matthews, S. Harney, J. Boney, J. F. Schetzina, J. D. Jenson, K. W. Dang, C. Terrill, T. Nohava, W. Yang, and S. Krishnankutty. *MRS Internet J. Nitride Semicond.* **4**, 9 (1999).
- [30] N Biyikli, I Kimukin, O Aytur, E Ozbay, *Photon. Tech. Lett.* **16**, 1718 (2004).
- [31] P. Kung, X. Zhang, D. Walker, A. Saxler, J. Piotrowski, A. Rogalski, M. Razeghi *Appl. Phys. Lett.* **67**, 3792 (1995).